AGU PUBLICATIONS

JGR

Journal of Geophysical Research: Atmospheres

RESEARCH ARTICLE
10.1002/2016JD026368

Key Points:
- Vertical wavelength, period, and vertical phase speed characterized with 5 years of Antarctic lidar data show lognormal distributions
- Vertical wavelength and period vary from summer minimum to winter maximum and exhibit linear correlations with background stratospheric wind
- Vertical wave number spectra have power spectral density decreasing from winter maximum to summer minimum for vertical wavelengths of 5–20 km

Correspondence to:
X. Chu,
xinzhao.chu@colorado.edu

Citation:
Zhao, J., X. Chu, C. Chen, X. Lu, W. Fong, Z. Yu, R. Michael Jones, B. R. Roberts, and A. Dörnbrack (2017), Lidar observations of stratospheric gravity waves from 2011 to 2015 at McMurdo (77.84°S, 166.69°E), Antarctica: 1. Vertical wavelengths, periods, and frequency and vertical wave number spectra, *J. Geophys. Res. Atmos.*, *122*, 5041-5062, doi:10.1002/2016JD026368.

Received 11 DEC 2016
Accepted 15 APR 2017
Accepted article online 20 APR 2017
Published online 16 MAY 2017

Lidar observations of stratospheric gravity waves from 2011 to 2015 at McMurdo (77.84°S, 166.69°E), Antarctica: 1. Vertical wavelengths, periods, and frequency and vertical wave number spectra

Jian Zhao[1,2], Xinzhao Chu[1,2], Cao Chen[1,2], Xian Lu[1,3], Weichun Fong[1,2], Zhibin Yu[1,2], R. Michael Jones[1], Brendan R. Roberts[1,2], and Andreas Dörnbrack[4]

[1]Cooperative Institute for Research in Environmental Sciences, University of Colorado Boulder, Boulder, Colorado, USA, [2]Department of Aerospace Engineering Sciences, University of Colorado Boulder, Boulder, Colorado, USA, [3]Department of Physics and Astronomy, Clemson University, Clemson, South Carolina, USA, [4]Institut für Physik der Atmosphäre, DLR Oberpfaffenhofen, Oberpfaffenhofen, Germany

Abstract Five years of atmospheric temperature data, collected with an Fe Boltzmann lidar by the University of Colorado group from 2011 to 2015 at Arrival Heights, are used to characterize the vertical wavelengths, periods, vertical phase speeds, frequency spectra, and vertical wave number spectra of stratospheric gravity waves from 30 to 50 km altitudes. Over 1000 dominant gravity wave events are identified from the data. The seasonal spectral distributions of vertical wavelengths, periods, and vertical phase speeds in summer, winter, and spring/fall are found obeying a lognormal distribution. Both the downward and upward phase progression gravity waves are observed by the lidar, and the fractions of gravity waves with downward phase progression increase from summer ~59% to winter ~70%. The seasonal and monthly mean vertical wavelengths and periods exhibit clear seasonal cycles with vertical wavelength growing from summer ~5.5 km to winter ~8.5 km, and period increasing from summer ~4.5 h to winter ~6 h. Statistically significant linear correlations are found between the monthly mean vertical wavelengths/periods and the mean zonal wind velocities from 30 to 50 km. Assuming horizontal phase speeds independent of month, the monthly mean horizontal wavelengths, intrinsic periods, and group velocities are estimated for stratospheric gravity waves. The slopes of wave frequency spectra change from −1.9 at 30–60 km to −1.45 around 60–65 km. The vertical wave number spectra show the power spectral density at vertical wavelengths of 5–20 km decreasing from winter maximum to summer minimum. Several aforementioned features are observed for the first time in Antarctica.

Plain Language Summary Generated by buoyancy force, gravity waves are one of the most ubiquitous and important atmospheric waves. They transport momentum and energy over the globe, affect the atmospheric circulation and chemical reactions, generate turbulence, and mix the air. The missing gravity wave drag especially in the Antarctic stratosphere is regarded as one possible mechanism for the long-lasting "cold-pole" problem in most climate models, and the challenge came from the sparsity of polar gravity wave observations. Five years of Fe Boltzmann lidar observations at McMurdo, Antarctica, provide a unique opportunity to meet this challenge and reveal numerous gravity wave properties for the first time in Antarctica. From these observational facts, the science points in the paper lead to a better understanding of the potential wave sources and provide information for gravity wave parameterization, a key point for atmospheric models to be right. In addition, a new method is rigorously developed to infer the intrinsic period, horizontal phase speed, and wavelength from the nearly linear relation of gravity wave parameters with the mean background winds. Overall, a complete picture of gravity waves in the polar stratosphere resolvable from lidar starts to emerge and would greatly impact the whole atmosphere community.

1. Introduction

Internal gravity waves are known to play essential roles in influencing the atmospheric circulation, thermal structures, composition, and variability through transporting momentum and energy among stratified layers from the troposphere to the thermosphere [e.g., *Lindzen*, 1981; *Holton*, 1982; *Hitchman et al.*, 1989;

Fritts and Alexander, 2003]. A general picture of gravity wave propagation was depicted by *C. Hines* in 1960s for waves generated at lower levels of the atmosphere with a range of spectra. The effects of amplification, reflection, intermodulation, and dissipation act to change the wave spectra continuously with increasing altitude and result in different dominant modes at different altitudes [*Hines*, 1960, 1964, 1974]. There are a variety of gravity wave sources such as wind flow over topography, deep convection, wind shears, jet streams, geostrophic adjustment, body forces created by wave dissipation, and wave-wave interactions [e.g., *Zhu and Holton*, 1987; *Alexander and Pfister*, 1995; *Vadas et al*., 2003; *Fritts et al*., 2006; *Alexander and Holton*, 2004; *Sato and Yoshiki*, 2008; *Vadas et al*., 2009; *Liu et al*., 2014; *Mzé et al*., 2014; *Eckermann et al*., 2016; *Smith et al.,* 2016]. Related research in characterizing gravity wave features, tracing the wave source and propagation, evaluating their impacts, etc., has been ongoing over many decades, yet large uncertainties and discrepancies still exist. Poor gravity wave parameterizations in numerical weather prediction and climate research models still present a major issue in these models [e.g., *Kim et al*., 2003; *McLandress et al*., 2006; *Alexander et al*., 2010; *Richter et al*., 2010; *Garcia et al*., 2014; *Mzé et al*., 2014]. For example, most of the General Circulation Models (GCMs) and Chemistry Climate Models (CCMs) have the cold pole problem; i.e., the simulated winter polar temperatures in the stratosphere are much colder than observed [e.g., *Hamilton et al*., 1999; *McLandress et al*., 2012]. Numerical simulations have indicated missing gravity wave drag in the southern stratosphere as a possible cause [*McLandress et al*., 2012; *Tan*, 2012; *Alexander and Grimsdell*, 2013]. Polar stratospheric gravity waves are also expected to have strong impacts on the composition and chemistry in this region because the temperature perturbations induced by these waves can potentially alter the rates of chemical reactions and, therefore, the concentrations of important atmospheric constituents such as ozone [*Lee et al*., 2014] and the formation of polar stratospheric clouds [*Steele et al*., 1983; *McDonald et al*., 2009]. It is crucial to characterize gravity waves in the stratosphere from a variety of observations, especially in the polar regions. Such observations will help improve our understanding of gravity wave characteristics and place parameterizations on a physical basis, which help improve the diagnostic and predictive capabilities of the current numerical models of the stratosphere and above.

The stratosphere above 30 km at McMurdo (77.8°S, 166.7°E), Antarctica, was regarded as a gap region for gravity wave studies before the McMurdo lidar campaign was started in late 2010 [*Chu et al*., 2011a]. Most observations of gravity waves over Antarctica, made with multiple instruments such as lidar, radar, balloon radiosonde, airglow imager, and GPS radio occultation, focused in regions either below 30 km or above 80 km [e.g., *Collins et al*., 1994, 1996; *Collins and Gardner*, 1995; *Moffat-Griffin et al*., 2011, 2013; *Espy et al*., 2004, 2006; *Hibbins et al*., 2007; *Tsuda et al*., 2000; *Baumgaertner and McDonald*, 2007; *Yoshiki and Sato*, 2000]. A large amount of recent activity in the atmospheric gravity wave community has been focused on studies over the Antarctic. Two superpressure balloon campaigns, VORCORE and CONCOREDIASI, were designed to detect the lower stratospheric gravity waves around or below 20 km [*Hertzog et al*., 2007; *Rabier et al*., 2012]. Momentum fluxes were derived from these balloon radiosonde measurements with lower (1 h or greater) and higher (12 min) resolutions for these two campaigns, respectively [*Hertzog et al*., 2008; *Walterscheid et al*., 2016]. The peak flux over the Antarctica Peninsula is averaged to be ~ −375 mPa during CONCOREDIASI campaign, which is ~10 times the campaign-averaged zonal flux for the VORCORE campaign [*Walterscheid et al*., 2016]. Satellite AIRS (Atmospheric Infrared Sounder) observations provide extensive data sets for global studies of stratospheric gravity waves. *Alexander and Barnet* [2007] discussed how satellite observations like AIRS could be used to constrain parameterizations of gravity waves in global models. A statistical study based on AIRS data for the region near the Patagonian Andes of South America and northernmost Antarctic Peninsula during September 2003 reveals that horizontal wavelengths range from ~30 to 500 km with a peak of ~100 km, while wave propagation angles from the background horizontal wind range from ~90 to 270° with a peak of ~190° [*Alexander and Barnet*, 2007]. *Hoffmann and Alexander* [2009] developed a data retrieval scheme for AIRS that made it feasible to study small-scale gravity waves with vertical wavelengths as short as 20 km. *Gong et al.* [2012] studied climatology of the gravity-wave-induced temperature variance at pressure levels from 2 to 100 hPa (~16–41 km) with AIRS measurements and demonstrated AIRS capable of detecting gravity waves with short vertical wavelengths (~12 km). Efforts were also spent on forming a global view of stratospheric gravity wave hotspots and discriminating gravity waves between orographic and nonorographic sources [*Hoffmann et al*., 2013, 2016]. However, the difficulty in interpreting satellite observations of gravity wave activity and their coarse vertical resolutions mean that to examine the region between 30 and 80 km requires detailed measurements by ground-based

Table 1. Statistics on Observational Lengths (in Hours) for Individual Month From 2011 to 2015

	Jan	Feb	Mar	Apr	May	Jun	Jul	Aug	Sep	Oct	Nov	Dec	Total
2011	82	85	36	40	59	72	54	67	14	38	148	160	855
2012	108	95	19	26	53	72	21	26	49	98	96	49	712
2013	90	19	49	99	45	71	83	63	47	53	91	145	855
2014	137	41	54	30	126	104	79	34	31	82	50	130	898
2015	61	51	57	52	66	121	104	42	67	48	14	81	764
Total	478	291	215	247	349	440	341	232	208	319	399	565	4084

instruments. Lidar observations have characterized the stratospheric gravity waves above 30 km at the South Pole and Rothera (67.5°S) [*Yamashita et al*., 2009; *Chu et al*., 2009] and at Davis (69°S) [*Alexander et al*., 2011; *Kaifler et al*., 2015], but there was a big latitudinal gap between the South Pole and Antarctic Circle. Lidar observations at McMurdo were chosen to fill in this important observational gap, which is the subject of the present study.

Ever since the McMurdo lidar campaign was initiated by the University of Colorado, many scientific findings have resulted from this unique observational data set with gravity waves playing important roles among all. For example, *Chu et al.* [2011b] discovered the thermospheric Fe layer events in the altitudes of 100–200 km, in which gravity waves were found to play an important role in the formation of such metal layers at McMurdo [*Chu et al*., 2011b; *Chu and Yu*, 2017]. Persistent, dominant and large-amplitude gravity waves with periods of 3–10 h and vertical wavelengths of ~20–30 km are discovered in the mesosphere and lower thermosphere (MLT) region from Fe lidar temperature measurements by *Chen et al.* [2013, 2016]. The sources of these inertia-gravity waves are still unknown. The obvious downward phase progression of these persistent waves indicates that the sources possibly lie in the lower atmosphere such as the stratosphere. *Chen et al.* [2016] analyzed the frequency spectra of the discovered inertia-gravity waves in the MLT in order to find a clue of the source region. The steeper slopes in the lower MLT compared to the fully damped theoretical slopes in the upper MLT suggest a likely wave source in the stratosphere or the lower mesosphere. All the above discoveries urge the need for characterizing the stratospheric gravity waves at McMurdo. Furthermore, *Lu et al.* [2015a] studied the vertical evolution of gravity wave potential energy densities and vertical wave number spectra from the stratosphere to the lower thermosphere at McMurdo but only for Antarctic winter months. It is therefore necessary to characterize stratospheric gravity waves through the entire year at McMurdo and compare with previous observations at the South Pole and Antarctic Circle. This kind of investigation may provide the possible link between the waves in the stratosphere and those in the thermosphere and to provide observational basis for future attempts of identifying the exact wave sources.

The present study is divided into two parts for the convenience of readers. In Part 1, we characterize the distributions of basic wave parameters along with the frequency spectra and vertical wave number spectra and also investigate how the seasonal variations of vertical wavelengths and periods are related to the background stratospheric winds. In Part 2, we characterize the gravity wave potential energy densities over five consecutive years and investigate the causes for their seasonal and interannual variations.

2. Methodology

2.1. Lidar Observational Campaign at Arrival Heights

The University of Colorado lidar group deployed an Fe Boltzmann temperature lidar [*Chu et al*., 2002; *Wang et al*., 2012] to Arrival Heights observatory near McMurdo in late 2010 [*Chu et al*., 2011a]. Ever since, the observational campaign has been ongoing for over 5 years, recording multiple parameters of the atmosphere from ~15 km to nearly 200 km, whenever weather permits [*Chu et al*., 2011a, 2011b, 2016]. Benefited from this long-lasting campaign, invaluable data sets were recorded for unraveling mysteries in the Antarctic atmosphere. Lidar temperature data from the pure Rayleigh scattering region (~30–70 km) are used in this study. This analysis covers a 5 year time period from 1 January 2011 to 31 December 2015.

Over the past 5 years, around 5000 h of data were accumulated owing to the hard work from our dedicated winter-over lidar students. Only 4084 h of data are chosen in this study as documented in Table 1 where the individual monthly observational lengths in hours are listed over the 60 months of studies. The total observational hours for each individual month vary from 14 to 160 h. Yearly and monthly

totals are also shown in this table. The data screening that results in such data statistics is largely based on the following criteria:

1. Only data sets with observational length equal to or longer than 6 h are chosen.
2. Data with large temporal gaps (4 h or above) are excluded in this study.
3. Data with low signal-to-noise ratios (SNRs) are excluded. Low SNRs usually occur during thin cloud coverage or high solar background in summer.

The raw photon counts were collected in the temporal and spatial resolutions of 1 min and 48 m, respectively. During the data retrieval process that converts the raw photon counts to real temperature, different resolutions and altitude ranges are used for the purposes of investigating the different gravity wave parameters. Achieving sufficient SNRs while keeping resolutions as high as possible is the major driver behind these selections. In sections 3 and 4, temperature data were retrieved with a temporal integration window of 2 h and an altitudinal window of 0.96 km to retain range information in order to investigate the vertical wavelength, period, etc., when summer data with low SNRs were included. The display resolutions were set to 1 h and 0.96 km. In section 5, resolutions of 0.5 h by 0.96 km were used for the frequency spectrum studies with June data (high-quality, nearly zero solar background in Antarctic winter) in order to compare with the work of *Chen et al.* [2016], while the wave number spectrum studies through the entire year adhered to the resolutions of 2 h by 0.96 km. Similarly, the selection of different altitude ranges was also based on the needed SNR for specific topics. For the studies of vertical wavelength, period, phase speed, and vertical wave number spectrum covering the entire year, we chose the altitude range of 30–50 km in order to achieve sufficiently high SNRs in summer. Altitude range from 30 to 65 km was chosen for the studies of frequency spectra using the winter data in June only. As a matter of fact, during the wintertime, owing to the high SNRs, this lidar has the capability of probing atmospheric temperatures to as high as 70 km using Rayleigh integration technique [*Chu et al*., 2011b; *Fong et al*., 2014; *Chen et al*., 2016].

2.2. Analysis Methods to Derive Gravity Wave-Induced Perturbations

Five years of temperature data are used to analyze the gravity wave activities in the stratosphere and lower mesosphere over McMurdo. Among the significant amount of data accumulated from 2011 through 2015, there are long-lasting data sets with various durations (up to ~65 h). For this study we choose only data sets lasting or longer than 6 h as elaborated above. Except for the frequency and vertical wave number spectra in section 5, for the studies in sections 3 and 4, all the data sets longer than 12 h are divided into 12 h observational segments without overlaps in order to ensure reasonable statistics on gravity wave parameters while including gravity wave spectra as much as possible. As the inertial period at McMurdo is 12.24 h and gravity waves with periods of 3–10 h are persistently observed in the MLT region [*Chen et al*., 2016], 12 h segments are the best choice of window size in our case. In this process of division, if the remaining segment at the end has observational length less than 6 h, then this observational segment is abandoned. Hence, all the observational segments used in this study have data length equal to or longer than 6 h but equal to or shorter than 12 h. Owing to this division process, the total observational hours actually used in sections 3 and 4 are reduced to 3784 h as enumerated in Table 3. Note that the frequency spectra (*f*-spectra) are derived with zero padding to the longest data set (~65 h), while the vertical wave number spectra (*m*-spectra) are derived from individual altitude profiles at a temporal display resolution of 1 h. As a result, the screened data are used without division of segments in the *f*- and *m*-spectra.

The following procedure is implemented to estimate the gravity wave perturbations. As the inertia-gravity waves (IGWs) with periods of 3–10 h are persistent and dominant in the McMurdo MLT region [*Chen et al*., 2013, 2016; *Chen and Chu*, 2017] while the planetary waves (PWs) are clearly seen in the stratosphere [*Lu et al*., 2013; *Chen et al*., 2016], this procedure aims to keep the IGW spectra as full as possible but significantly filter out PWs and tides.

1. Temperature perturbations $\Delta T(z,t)$ are calculated through subtracting the temporal mean $T_0(z)$ of the 12 h segment at each altitude first and then subtracting the altitudinal mean at each time grid for every observational segment. Such altitudinal mean subtraction is to remove the nearly vertical stripes found in some segments of the Rayleigh temperature data, equivalently removing waves with long vertical wavelengths. Dividing the absolute temperature perturbations by the temporal mean gives the raw relative temperature perturbations before filtering.

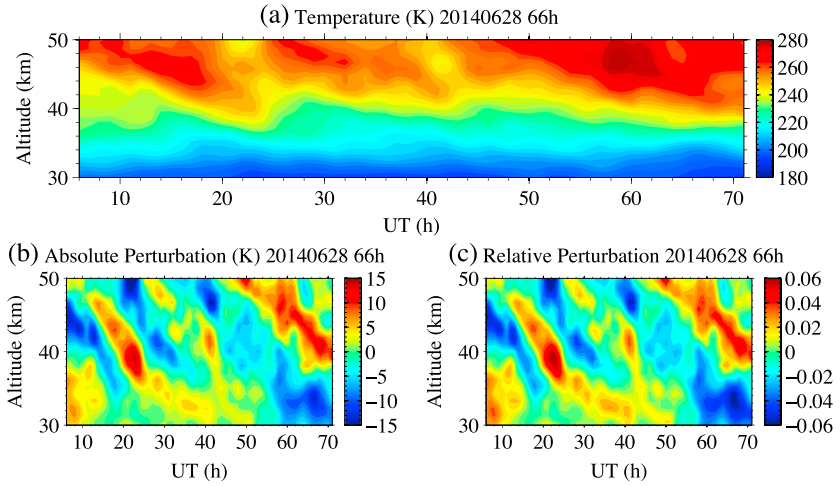

Figure 1. An illustration of data processing procedures before the high-pass filtering based on the observation on 28–30 June 2014. (a) Raw lidar temperatures (K) versus UT (h) and altitude (km). (b) Absolute (in unit of K) and (c) relative temperature perturbations are perturbations without high-pass filtering.

2. At each individual altitude, a high-pass filter in time domain is applied to the temperature perturbations obtained above to derive temporally filtered temperature perturbations. The high-pass filter is designed to remove waves with periods longer than 11 h, and it is implemented as the following. First, a one-dimensional fast Fourier transform (1DFFT) is applied to a time series to attain its frequency spectrum. Then a sixth-order Butterworth filter window is multiplied with the obtained frequency spectrum to remove frequency components outside the desired frequency range. Finally, an inverse 1DFFT is applied to this multiplied frequency spectrum to attain a new time series with only the selected frequency components.
3. At each individual time grid, by applying a high-pass filter in the altitudinal domain to the temporally filtered temperature perturbations, the final temperature perturbations $T'(z,t)$ are obtained. This filter and its implementation are identical to the high-pass filter used in Step (2) except it is designed to filter out waves with vertical wavelengths longer than 30 km.
4. The temporal mean $T_0(z)$ in Step (1) is considered as the temperature background, and the filtered relative temperature perturbations of every observational segment are calculated as

$$T'_{\mathrm{Rel}}(z,t) = T'(z,t)/T_0(z) \tag{1}$$

Figure 1 is an illustration of data processing procedures using the data set of 28–30 June 2014. Clear downward phase progression can be identified in both the absolute (Figure 1b) and raw relative (Figure 1c) temperature perturbations without high-pass filtering, which usually indicates upward energy propagation. Note that due to the lack of background wind information, the inferred upward or downward energy propagation here may have ambiguities. Strong wave signatures can be easily identified in these plots. As planetary wave components with periods over 1 day are dominant in the stratosphere [*Lu et al.*, 2013] and visible in the raw relative perturbations (Figure 1c), it is necessary to filter out waves with long periods and long vertical wavelengths as elaborated above in Steps (2) and (3) in order to derive pure gravity wave perturbations and minimize the contamination from planetary waves. An example result is shown in Figure 2a where gravity wave signatures show up clearly. The filtered relative temperature perturbations derived above represent the perturbations induced by gravity waves within certain ranges of frequency and vertical wave number spectra. Further analyses are performed on these perturbations in order to characterize the McMurdo gravity waves on various aspects. These data analysis methods are introduced before the results are presented in sections 3–5.

3. Characterization of Vertical Wavelength, Period, and Phase Speed

Characterizing gravity wave parameters, such as wavelength, period, phase speed, frequency spectra, vertical wave number spectra, and phase progression direction, for McMurdo has the potential to shed light on the

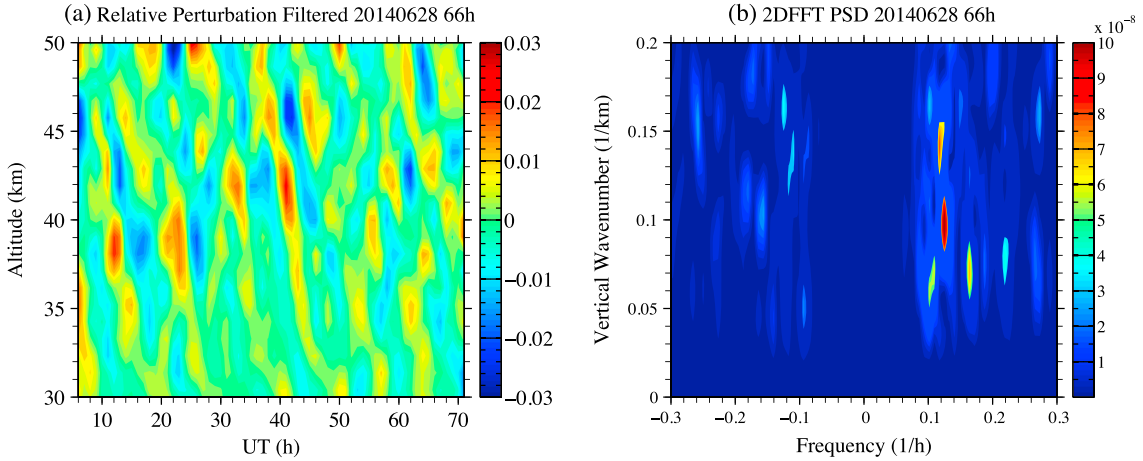

Figure 2. (a) High-pass filtered relative perturbations versus UT (h) and altitude (km). (b) Power spectral density versus frequency (1/h) and vertical wave number (1/km). The unit of the PSD is arbitrary. Both Figures 2a and 2b are based on the observation on 28–30 June 2014.

understanding of polar wave dynamics, e.g., in which specific way gravity waves are transporting momentum and energy, and how gravity wave properties change with the time of year. To derive the basic wave parameters, a two-dimensional fast Fourier transform (2DFFT) is first applied to the relative perturbations of segments to obtain the power spectral density (PSD). These PSD plots are then scaled by their corresponding temporal length and altitudinal range so that their magnitudes do not depend on the observational window lengths. The scaling is done through dividing the original PSD value on every grid point by the total temporal length and the total altitudinal range. We further convert these scaled PSD plots to area-preserving form through multiplying PSDs by their corresponding wave numbers and frequencies following the approaches in *Yamashita et al.* [2009] and *Tsuda et al.* [2000]. The spectral noise floor of the area-preserving PSD, induced by the lidar measurement errors, is estimated using the Monte Carlo method described below. First, 1000 Gaussian white noise simulation data are constructed at each grid point of the measurement (time versus altitude) with a standard deviation equal to the measurement error at that grid point. Then, we run each of the above constructed 1000 sets of 2-D simulation data through the same filtering and 2DFFT processes to obtain their corresponding area-preserving PSD. Finally, the spectral noise floor is estimated by taking the mean of these 1000 simulated noise spectra. The spectral noise floor obtained above is then subtracted from the measured 2DFFT power spectrum. The number of 1000 is chosen with the consideration of computational expenses. In fact, the noise floor barely varies once this number exceeds 500. Figure 2 shows an example of the filtered relative perturbations and its area-preserving PSD plot on 28–30 June 2014 with the spectral noise floor subtracted already. Note that as an example of illustrating the procedures to derive relative perturbations and PSD, we did not divide this observation into 12 h segments in Figures 1 and 2. However, this observation is actually divided into 12 h segments for the study below as is done for all the other observations.

2DFFT spectral analysis is capable of distinguishing the gravity wave vertical phase progression directions (upward or downward) [e.g., *Yamashita et al.*, 2009; *Lu et al.*, 2015b, 2016]. Our 2DFFT formalism leads to the fact that the spectral peaks with positive frequencies correspond to downward phase progression waves, while the peaks with negative frequencies represent upward phase progression, with the vertical wave numbers being positive. Using Figure 2b as an example, there are several downward phase progression waves with the strongest peak locating at a positive frequency of ~0.13 h^{-1} and a vertical wave number of ~0.10 km^{-1}. In comparison, the upward phase progression waves with negative frequencies have much lower power spectral densities in this particular example. In this study, the first three dominant waves (among both upward and downward phase progression wave fields) above the spectral noise floor are picked in every one of these area-preserving PSD plots in order to identify the signatures of dominant gravity waves. The choice of three waves is to align in accordance with the statistical studies performed by *Yamashita et al.* [2009] for the South Pole and Rothera. Table 2 summarizes the total number of waves identified from all the qualified 12 h segments through 5 years from 2011 to 2015, which amount to 1062 waves. The corresponding numbers of ground-relative downward and upward phase progression waves in the

Table 2. Gravity Wave Propagation Direction in the 30–50 km at McMurdo

	Total Number of Waves	Downward Phase Progression	Upward Phase Progression	Downward Phase to Total Wave Ratio
Summer	462	273	189	59.1%
Winter	348	245	103	70.4%
Spring + Fall	252	160	92	63.5%
Total	1062	678	384	63.8%

seasons of summer, winter, and "spring + fall" are also given in Table 2. The seasons are defined as summer from November through February, winter from May through August, fall for March and April, and spring for September and October. The fractions of downward phase progression waves out of the total waves in the individual seasons, range from ~59% in summer to ~70% in winter, with an overall average of ~64%. The trend of increasing fraction of downward phase progression waves from summer to winter is consistent with the observations at Rothera by *Yamashita et al.* [2009]. Note that the ground-relative (not intrinsic) frequency is inferred from the lidar data only.

The statistical studies are conducted on the spectra of the 1062 dominant gravity waves identified above, including both downward and upward phase progression waves. Histograms in Figure 3 illustrate the seasonal distributions of vertical wavelengths λ_z, ground-relative periods τ, and vertical phase speeds c_z. For the convenience of presentation, parameters (λ_z, τ, and c_z) of downward phase progression waves are plotted as positive values in Figure 3, while the negative values are for upward phase progression waves. The vertical wavelengths of dominant gravity waves distribute from a few to less than 20 km, while the dominant wave periods (ground-relative) range from ~3 to ~10 h. The vertical phase speeds vary from ~0.1 to ~1 m/s. The means, standard errors, and standard deviations of all individual distributions are summarized in Table 3, in which all numbers are presented in positive values of their magnitudes. The medians are also provided in Table 3. It is obvious from Table 3 that the vertical wavelengths and periods increase in winter as shown by the mean and the median values; i.e., λ_z grows from ~5.5 km in summer to ~8 km in winter while τ increases from ~4.5 h in summer to ~5.7 h in winter. Such seasonal variations can be seen for both the downward and upward phase progression waves. There are slight increases in the vertical phase speeds in winter, but not as obvious as λ_z and τ. The seasonal variations of λ_z and τ will be further investigated in section 4. Comparing our results to those by *Yamashita et al.* [2009], both the vertical wavelengths (~7.1 km) and periods (~5.3 h) at

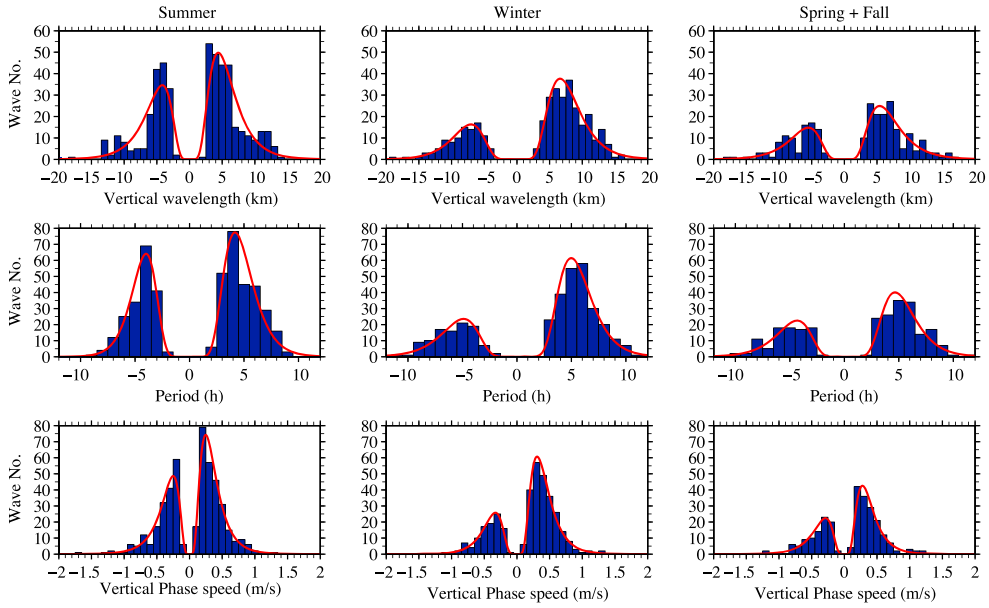

Figure 3. Seasonal distributions of (top row) vertical wavelength (km), (middle row) period (h), and (bottom row) vertical phase speed (m/s). For each panel, *y* axis shows number of waves. Positive values denote waves with downward phase progression whereas negative values denote waves with upward phase progression.

Table 3. Statistics on Seasonal Distributions of Vertical Wavelength, Period, and Vertical Phase Speed[a]

		Summer	Winter	Spring + Fall	Mean/Total[c]
λ_z (km) mean ± Std. error (Std. deviation)	Downward[b]	5.97 ± 0.17 (2.86)	8.07 ± 0.18 (2.88)	7.14 ± 0.25 (3.18)	7.06
	Upward	5.85 ± 0.24 (3.26)	8.35 ± 0.29 (2.94)	7.12 ± 0.32 (3.10)	7.11
Median	Downward	5.26	7.68	6.60	6.51
	Upward	4.84	7.93	6.09	6.29
Skewness, kurtosis	Downward	0.98, −0.09	0.48, −0.52	0.95, 0.39	
	Upward	1.87, 4.87	0.99, 1.13	1.15, 1.41	
τ (h) mean ± Std. error (Std. deviation)	Downward	4.86 ± 0.09 (1.53)	5.72 ± 0.11 (1.73)	5.44 ± 0.14 (1.72)	5.34
	Upward	4.50 ± 0.10 (1.32)	5.78 ± 0.18 (1.83)	5.21 ± 0.19 (1.79)	5.16
Median	Downward	4.57	5.57	5.33	5.16
	Upward	4.13	5.57	5.02	4.91
Skewness, kurtosis	Downward	0.43, −0.68	0.58, 0.14	0.48, 0.03	
	Upward	0.82, 0.27	0.27, −0.53	0.47, −0.48	
C_z (m/s) mean ± Std. Error (Std. Deviation)	Downward	0.37 ± 0.01 (0.21)	0.43 ± 0.01 (0.21)	0.39 ± 0.02 (0.21)	0.40
	Upward	0.39 ± 0.02 (0.24)	0.44 ± 0.02 (0.20)	0.42 ± 0.02 (0.22)	0.42
Median	Downward	0.32	0.39	0.34	0.35
	Upward	0.32	0.39	0.36	0.36
Skewness, kurtosis	Downward	1.44, 2.32	1.35, 2.65	1.59, 2.92	
	Upward	1.97, 5.37	1.09, 0.98	1.26, 1.55	
Observation hours		1633	1261	890	3784

[a] λ_z, τ, and C_z represent vertical wavelength, ground-relative period, and vertical phase speed. Shown as mean ± standard error (Std. error), standard deviation (Std. deviation), median, skewness, and kurtosis.
[b] The downward and upward represent downward and upward phase progressions of gravity waves, respectively.
[c] Regarding the mean/total column, mean is for rows of λ_z, τ, and C_z, and total is for the row of observation hours.

McMurdo are generally longer than those at the South Pole (~4.1 km and ~1.7 h) and Rothera (~4.4 km and ~1.8 h) while the vertical phase speeds (~0.4 m/s) at McMurdo are slower than those at the South Pole and Rothera (~0.7 m/s). Such differences are likely due to the fact that different spectra of gravity waves are selected in these two studies. Gravity waves with periods of ~1–6 h and vertical wavelength of 2–30 km are included in *Yamashita et al.* [2009], whereas here we focus on waves with periods of ~2–11 h and vertical wavelength of ~2–30 km. The differences could also be due to different excitation mechanisms that generate gravity waves with different spectral characteristics.

The individual distributions in Figure 3 obviously deviate from normal distributions. To quantify such features, we calculate the skewness and kurtosis for each distribution via equations (2) and (3). Skewness is the third moment—a measure of asymmetry of a probability distribution around its mean, and Kurtosis is the fourth moment—a measure of the peakedness or flatness relative to a normal distribution [*Press et al.*, 1986; *Chu et al.*, 2006].

$$\text{Skewness}(x_1,\ \ldots,\ x_i,\ \ldots,\ x_N) = \frac{1}{N}\sum_{i=1}^{N}\left(\frac{x_i-\bar{x}}{\text{std}}\right)^3 \tag{2}$$

$$\text{Kurtosis}(x_1,\ \ldots,\ x_i,\ \ldots,\ x_N) = \frac{1}{N}\sum_{i=1}^{N}\left(\frac{x_i-\bar{x}}{\text{std}}\right)^4 - 3 \tag{3}$$

where $\bar{x}$ is the mean of values $x_1, \ldots, x_i, \ldots, x_N$, std is the standard deviation of the distribution, and N is the number of data points. The standard errors of the skewness and kurtosis for a normal distribution are approximately $\sqrt{6/N}$ and $\sqrt{24/N}$, respectively. Taking the winter downward phase progression c_z as an example of the skewness and kurtosis in Table 3, with 68% confidence level, we have skewness 1.35 ± 0.16, and kurtosis 2.65 ± 0.31; with 95% confidence level, we have skewness 1.35 ± 0.32, and kurtosis 2.65 ± 0.62. The statistics in Table 3 reveal that the distributions in Figure 3 clearly deviate from normal distributions.

Given that previous observations have shown lognormal distributions of gravity wave momentum flux and potential energy density [*Alexander et al.*, 2008; *Hertzog et al.*, 2012; *Baumgaertner and McDonald*, 2007; *Murphy et al.*, 2014], we test if the histograms in Figure 3 are also lognormally distributed. The lognormal distribution defined by equation (4)

Table 4. Parameters of the Lognormal Fittings[a] to Histograms in Figure 3

			μ[c]	σ	A	Correlation[d]	MPV[e]
λ_z (km)[b]	Summer	Down[f]	1.40 ± 0.05[g]	0.43 ± 0.04	58	94%	4.1
		Up	1.39 ± 0.07	0.32 ± 0.05	38	96%	4.0
	Winter	Down	1.88 ± 0.04	0.41 ± 0.04	36	97%	6.5
		Up	1.91 ± 0.06	0.36 ± 0.04	14	98%	6.8
	Spring	Down	1.65 ± 0.07	0.45 ± 0.04	28	94%	5.2
	+ Fall	Up	1.67 ± 0.08	0.42 ± 0.05	16	90%	5.3
τ (h)	Summer	Down	1.39 ± 0.04	0.37 ± 0.03	65	98%	4.0
		Up	1.36 ± 0.04	0.29 ± 0.03	46	99%	3.9
	Winter	Down	1.62 ± 0.04	0.33 ± 0.02	47	98%	5.0
		Up	1.62 ± 0.06	0.37 ± 0.04	20	98%	5.0
	Spring	Down	1.53 ± 0.05	0.38 ± 0.03	34	96%	4.6
	+ Fall	Up	1.44 ± 0.08	0.41 ± 0.05	21	94%	4.2
C_z (m/s)	Summer	Down	−1.46 ± 0.06	0.54 ± 0.04	101	99%	0.23
		Up	−1.46 ± 0.07	0.49 ± 0.05	68	98%	0.23
	Winter	Down	−1.18 ± 0.06	0.50 ± 0.04	72	100%	0.31
		Up	−1.17 ± 0.08	0.49 ± 0.05	30	99%	0.31
	Spring	Down	−1.36 ± 0.08	0.51 ± 0.05	55	99%	0.26
	+ Fall	Up	−1.32 ± 0.10	0.53 ± 0.07	30	98%	0.27

[a]The lognormal fitting function is $h(x) = \frac{A}{\sqrt{2\pi}\sigma} \exp\left[-\frac{(\ln(x)-\mu)^2}{2\sigma^2}\right]$.
[b]λ_z, τ, and C_z represent the vertical wavelength, ground-relative period, and vertical phase speed, respectively.
[c]A, μ, and σ represent the amplitude, mean, and standard deviation of the variable's natural logarithm, respectively.
[d]Correlation denotes the correlation coefficient of the lognormal fitting.
[e]MPV denotes the most probable value of the lognormal distribution.
[f]Down and up represent downward and upward phase progressions of gravity waves.
[g]The lognormal fittings and correlations are done at 95% confidence level.

$$h(x) = \frac{A}{\sqrt{2\pi}\sigma} \exp\left[-\frac{(\ln x - \mu)^2}{2\sigma^2}\right] \tag{4}$$

is fitted as the red lines in Figure 3. The fitting parameters μ, σ, and A are summarized in Table 4. The correlation coefficients for these lognormal fittings are very high, ranging from 90% to 100% at 95% confidence level. It is therefore unequivocal that the observed λ_z, τ, and c_z are lognormally distributed at McMurdo. Under the definition of lognormal distribution in equation (4), the most probable value (MPV) is given by $x_{MPV} = e^{\mu}$, which is summarized in Table 4. The trends of vertical wavelengths and ground-relative periods increasing from the summer minima to the winter maxima also clearly show up in the most probable values. Comparing Table 4 with Table 3, we find that the MPV, median, and mean values have the following relation: $x_{MPV} < x_{median} < x_{mean}$. This fact is consistent with the lognormal distributions that are highly skewed toward lower values as we have characterized from the lidar observations.

4. Vertical Wavelengths and Periods Versus Background Stratospheric Winds

To further investigate the seasonal variations of λ_z and τ, the monthly means and standard errors of wave parameters averaged over the 5 year analysis period are plotted in Figure 4. The monthly means are calculated by taking the means of certain wave parameters from all the individual gravity waves in a particular month through all 5 years. Blue (red) lines in these plots correspond to downward (upward) phase progression waves. Figure 4a shows clearly that the vertical wavelength increases when approaching winter and decreases as returning to summer. Vertical wavelength reaches its peak of 8.8 ± 0.69 km in June for upward phase progression waves and of 8.6 ± 0.51 km in August for downward phase progression waves. The dominant periods follow a similar annual cycle with the winter peak values of nearly 6 h while the summer values in December and January are of ~4.5 h as shown in Figure 4b. As the case for dominant vertical phase speeds, they roughly remain constant (~0.4 m/s) throughout the year. Because sufficient numbers of gravity waves were recorded for each month over the 5 years of lidar observations, the errors associated with the derived wave parameters are small enough that the observed seasonal variations of λ_z and τ are statistically significant.

Next we investigate whether the seasonal variations of λ_z and τ are related to the mean background winds in the stratosphere [*Whiteway et al.*, 1997; *Alexander et al.*, 2011]. For this purpose, the European Centre for

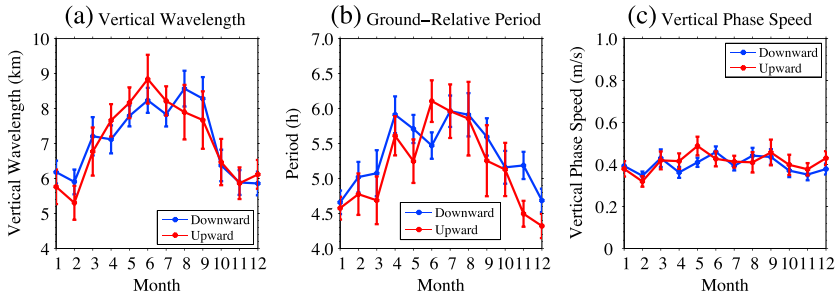

Figure 4. Monthly mean (a) vertical wavelengths, (b) periods, and (c) vertical phase speeds for gravity waves with downward (blue) and upward (red) phase progression. The error bars represent the standard errors, which are equal to the standard deviations divided by the square root of the numbers of independent samples.

Medium-Range Weather Forecasts (ECMWF) model [*Dee et al.*, 2011] is invoked to provide wind information. The ECMWF model outputs four wind profiles per day near McMurdo station, so there are ~120 wind profiles per month. Figure 5 is an illustration of monthly mean zonal and meridional wind profiles from ECMWF at McMurdo averaged over 5 years from 2011 through 2015. We group λ_z observations with their corresponding total horizontal wind speeds (daily averages of the observational segments) at 40 km from ECMWF. Figures 6a and 6b shows the probability density functions and cumulative distribution functions of λ_z grouped by wind speed larger than 40 m/s and smaller than 20 m/s. The results can be summarized as that with higher stratospheric winds, waves tend to have longer vertical wavelengths.

We further look into the correlation coefficients between the monthly mean vertical wavelengths (shown in Figure 4) and the monthly mean zonal and meridional wind velocities in the stratosphere, respectively. The monthly mean wind velocities are obtained by averaging the zonal and meridional winds, respectively, from 30 to 50 km in the monthly mean profiles of Figure 5. The vertical wavelengths λ_z are plotted against the mean zonal winds in Figures 6c and 6d, and against the mean meridional winds in Figures 6e and 6f, where the green lines represent the linear regressions with both *x* and *y* axis errors considered using the York Curve fitting method [*York et al.*, 2004]. Fitting parameters are summarized in Table 5. For downward phase progression waves, the vertical wavelength and the mean zonal wind velocity correlate at 0.88 at 95% confidence level. The linear fitting curve has a slope of 39.8 ± 5.1 m/(m/s) and an intercept of 6.22 ± 0.15 km at zero zonal wind. For upward phase progression waves, they correlate at 0.83 at 95% confidence level. The linear fitting curve has a slope of 45.6 ± 7.0 m/(m/s) and an intercept of 6.11 ± 0.20 km at zero zonal wind. In the case of λ_z

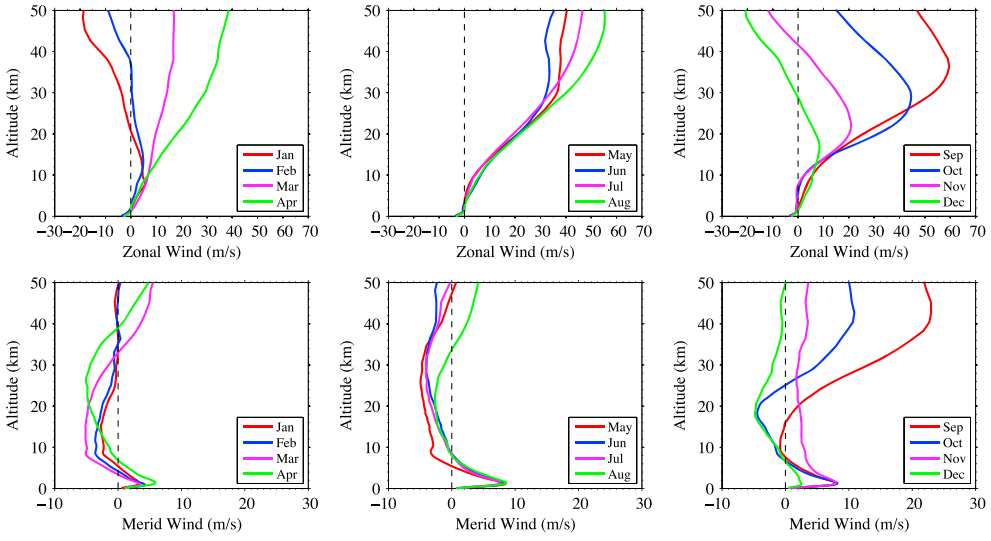

Figure 5. Monthly (top row) mean zonal and (bottom row) meridional wind profiles averaged over 5 years from 2011 through 2015 using ECMWF data at McMurdo, Antarctica.

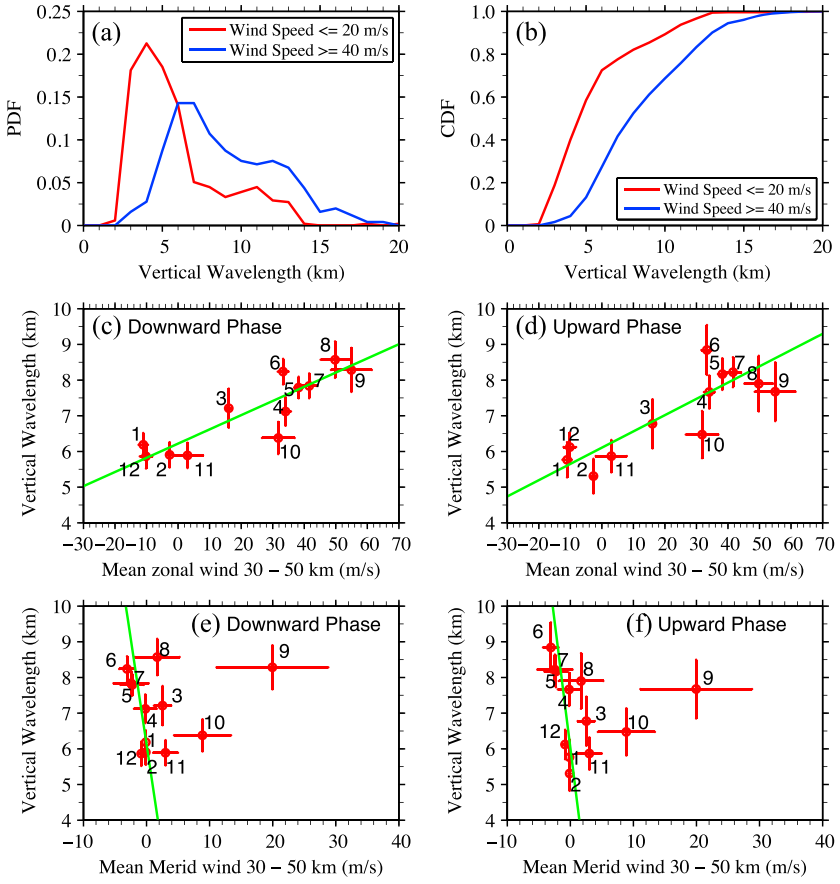

Figure 6. (a) Probability density functions (PDF) and (b) cumulative distribution functions (CDF) for vertical wavelength distribution under different wind conditions at 40 km. (c and d) The correlations of the monthly mean vertical wavelengths with the monthly mean zonal wind velocities in the stratosphere (30–50 km) for downward and upward phase progression waves. (e and f) The correlations of vertical wavelengths with the monthly mean meridional winds. The green lines show the linear regressions with both *x* and *y* axis errors considered. The numbers in Figures 6c–6f denote the month of each individual data point. Note that the September data points are excluded in the linear regressions in Figures 6e and 6f.

versus the mean meridional winds, the linear regressions lead to the λ_z intercepts of 6.14 ± 1.28 and 6.03 ± 1.37 km for downward and upward phase progression waves, respectively. However, the correlation coefficients are low, less than 35% (see Table 5), which are likely caused by the meridional winds (except September data points) being much smaller than the corresponding zonal winds, while the variances associated with the meridional winds are large over 5 years at McMurdo. Such large wind variances make

Table 5. Parameters Inferred From Figures 6 and 7[a]

	Zonal Wind		Meridional Wind[b]	
	Downward	Upward	Downward	Upward
S_{λ_z} (m/(m/s))	39.8 ± 5.1	45.6 ± 7.0	−1178 ± 613	−1419 ± 643
Intercept (km)	6.22 ± 0.15	6.11 ± 0.20	6.14 ± 1.28	6.03 ± 1.37
Correlation for λ_z	88.3%	83.2%	−25.8%[b]	−33.6%[b]
S_τ (s/(m/s))	67.7 ± 10.1	84.6 ± 13.0	−5280 ± 3728	−2746 ± 1380
Intercept (h)	4.94 ± 0.08	4.67 ± 0.09	4.57 ± 1.28	4.51 ± 1.16
Correlation for τ	87.8%	80.7%	−24.5%[b]	−30.8%[b]
c_h (m/s)	21.2	20.8		
cos(θ)	−0.14	−0.16		

[a]In the calculation, $N = 2.14 \times 10^{-2}$ rad/s and $H = 7$ km.
[b]Linear fittings for meridional winds exclude the September data points.

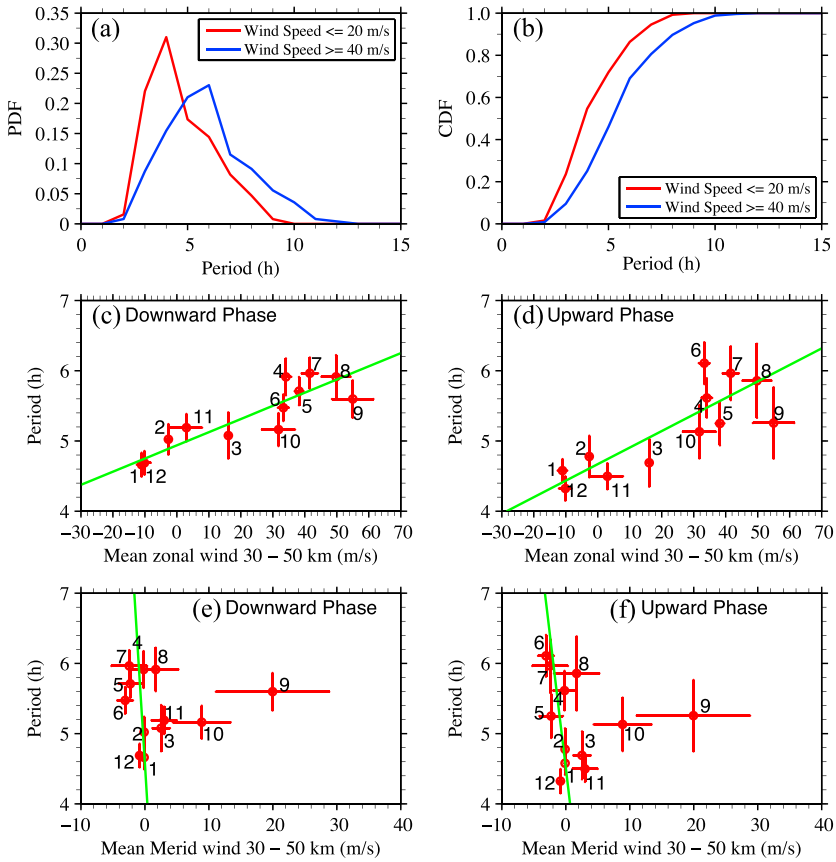

Figure 7. Same as Figure 6 except for the ground-relative periods.

it hard to show any definite relationship with the small meridonal wind velocities. Nevertheless, the zero-wind points in the mean zonal and meridional winds correspond to intercepted λ_z of ~6.1–6.2 km, comparable with each other. Such a result will be used in section 6 to estimate intrinsic properties.

Similar analyses are done to the ground-relative period τ versus the mean zonal and meridional wind velocities, respectively. Shown in Figures 7a and 7b are the probability density functions and cumulative distribution functions of periods grouped by total wind speed larger than 40 m/s and smaller than 20 m/s. Similar to the results for λ_z, waves tend to have longer periods under higher winds in the stratosphere. The 12 monthly mean periods are plotted against the mean zonal winds in Figures 7c and 7d, and against the mean meridional winds in Figures 7e and 7f. A similar linear regression (with both the *x* and *y* axis errors considered using the York Curve fitting method) is applied and shown as the green straight lines in Figures 7c–7f. Fitting parameters are summarized in Table 5. For downward phase progression waves, the period and the mean zonal wind velocity correlate at 0.88 at 95% confidence level. The linear fitting curve has a slope of 67.7 ± 10.1 s/(m/s) and an intercept of 4.94 ± 0.08 h at zero zonal wind. For upward phase progression waves, they correlate at 0.81 at 95% confidence level. The linear fitting curve has a slope of 84.6 ± 13.0 s/(m/s) and an intercept of 4.67 ± 0.09 h at zero zonal wind. Similar to the λ_z case, the meridional wind plots (Figures 7e and 7f) give low linear correlation coefficients, likely due to the small wind velocities but large variances. The zero-wind points in the mean zonal and meridional winds correspond to intercepted τ of ~4.5–4.9 h.

The 12 months of January through December are marked as the numbers from 1 to 12 in Figures 6c–6f as well as in Figures 7c–7f. It is clear from these figures that the six data points from April through September are "clustered" in the right upper corner of zonal wind plots, the four data points from summer months (December through February) are "clustered" toward the left-lower corner, and March and October are near the middle during transitions. Such summer to winter transition and vice versa are also seen in the ECMWF

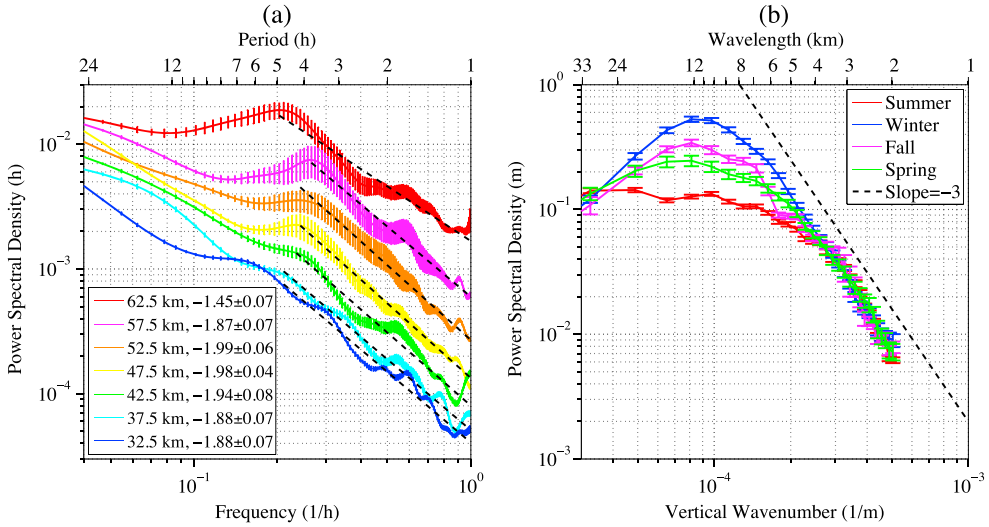

Figure 8. (a) Stratospheric gravity wave frequency spectra for different altitudes in June. Different colors represent different altitudes. The dashed black lines are linear fittings with their slopes given in the legends. (b) Power spectral density for vertical wave number spectra over different seasons (represented by different colors). The error bars are obtained as standard errors.

monthly mean wind profiles in Figure 5. Both the vertical wavelengths and ground-relative periods of both downward and upward phase progression waves show statistically significant linear correlations with the mean zonal winds. Such linear correlations will be further investigated in section 6. Overall, such linear correlations are stronger for the downward phase progression waves than for the upward phase progression waves, likely because more data points in the downward phase progression waves give better statistics than the upward phase progression case.

5. Frequency and Vertical Wave Number Spectra

We perform a frequency spectral study in the upper stratosphere at McMurdo, Antarctica, in order to compare with the observational results of wave frequency spectra in the MLT region reported by *Chen et al.* [2016]. For this comparison purpose, we take the following procedure identical to that used by *Chen et al.* [2016] but somewhat different from the one described in section 2. June data over the 5 years of 2011–2015 are chosen with the resolutions of 0.5 h by 0.96 km from 30 to 65 km. For this part of the study, we do not divide the observations into 12 h segments but leave them with their original observational time lengths as we wish to have long time series for frequency spectral analysis. For each observation, the temporal means are derived over the observation length at individual altitudes, and we calculate the relative temperature perturbations by subtracting the temporal means from the raw data and then dividing by the temporal means. The obtained relative perturbations are prewhitened with a fourth-order autoregressive model developed by *Chen et al.* [2016]. As the longest data set is 65 h, we zero pad the shorter data to 65 h before applying a 1DFFT to the prewhitened perturbations at individual altitudes. We then smooth the resulted raw PSDs using a Hamming window with the full width at half maximum (FWHM) of 0.1 h^{-1} to reduce the variability in the spectral slope estimation. Such smoothed PSDs are postcolored to obtain the real PSDs following *Chen et al.* [2016]. The real PSDs at individual altitudes are then vertically averaged over 5 km interval to reduce the variance in the spectra. Finally, the results for individual observations are weighted by their observational time lengths to obtain weighted-average frequency spectra. The mean smoothed frequency spectra are plotted at increments of 5 km from 32.5 to 62.5 km in Figure 8a. The error bars are calculated as the standard errors in the process of weighted averaging.

The dashed black lines in Figure 8a are the least-squares fittings of the PSDs in the frequency range from the characteristic frequency to 1 h^{-1} using a linear equation $\log_{10}(y) = a + b \times \log_{10}(x)$. Here the characteristic frequency is the transition frequency between the regions of positive and negative slopes in the PSD

spectra for altitudes above 40 km. As it is difficult to judge where the characteristic frequency is from 32.5 to 37.5 km, the fitting frequency range is set to 0.2–1 h^{-1} for these lower altitudes. The fitted spectral slopes, as indicated in the legends of Figure 8a, are about −1.9 from 30 to 60 km, which is close to the value of −1.8 obtained by *Hostetler and Gardner* [1994] for the upper stratosphere (25–40 km) at Kahalui, Maui. The frequency spectral slopes become much shallower (about −1.45) when the altitudes reach 60–65 km. We notice that the slopes in the stratosphere are generally shallower than those in the MLT, which range from −2.6 to −1.6 for 85–110 km [*Chen et al*., 2016]. The slopes in *Chen et al.* [2016] are derived with a uniform fitting range from 0.1 to 1 h^{-1}. According to *Fritts and Alexander* [2003], frequency spectra of horizontal wind and temperature typically vary as $\mathrm{PSD}(\omega) \sim \omega^{-p}$ (where ω is the wave frequency) with p varying from 1 to 2 between the inertial and buoyancy frequencies, and most $p \approx -5/3$. Our results in the stratosphere are within the 1–2 range but most of the slopes in the MLT fall outside this range [*Chen et al*., 2016].

Lu et al. [2015a] have studied PSDs in the vertical wave number domain for winters from 2011 to 2013 at McMurdo. We expand the study to four seasons from 2011 to 2015. The vertical wave number spectra over different seasons are plotted in Figure 8b. T'_{Rel} is used to calculate the vertical wave number spectra (data resolutions of 2 h by 0.96 km from 30 to 50 km over 5 years). We follow the procedures from *Dewan and Grossbard* [2000] and *Lu et al.* [2015a]. The power spectral density is derived using Discrete Fourier Transform (DFT) as

$$F(m_k) = \frac{\Delta z |f(m_k)|^2}{N_z} = \frac{\Delta z}{N_z}\left|\sum_{n=1}^{N_z} x(z_n) e^{-\frac{2\pi(n-1)(k-1)}{N_z} i}\right|^2 \tag{5}$$

where m_k is the kth wave number and $f(m_k)$ denotes its DFT value, Δz is the vertical interval of the data, and N_z is the total points of a single vertical profile. The parameter $x(z_n)$ is the relative temperature perturbation at altitude z_n, which is T'_{Rel} in our case. With current data resolutions, there are no apparent white noise floors at the high wave number end of the spectra. Therefore, noise floors were not subtracted from the obtained spectra, similar to the practice by *Gardner et al.* [1989], *Senft and Gardner* [1991], and *Lu et al.* [2015a]. We group the calculated PSDs into four seasons and average them within each season. The average is weighted by observational time length, and the error bars are calculated as the standard errors.

The characteristic vertical wave number m^*, which is the turning point of the slopes of the spectra, is ~0.08 km^{-1} in winter, fall, and spring, corresponding to a characteristic vertical wavelength of 12.5 km. There is no apparent characteristic vertical wave number in summer. For the short vertical wavelength spectrum, the PSDs remain almost the same over different seasons. The seasonal variations of PSDs show up substantially in the long vertical wavelength portion with a lowest level in summer, a highest level in winter, and medium levels in spring and fall. Since there exists an enhancement of PSDs in long vertical wavelength portion in winter, we would have more chances to observe gravity waves with longer vertical wavelengths, which is the case as elaborated in section 4. The dashed black line in Figure 8b is an indication of slope −3. The slopes of PSDs in all four seasons are close to −3 in the shorter vertical wavelength range. This result is similar to the studies done by *Allen and Vincent* [1995] and *Lu et al.* [2015a].

6. Discussion

We explore the linear correlations of λ_z and τ of gravity waves with the mean stratospheric winds in Figures 6 and 7 and attempt to infer the horizontal wavelengths and intrinsic periods of dominant gravity waves in the stratosphere. Our purpose is to use the information obtained to help judge if the dominant gravity waves in the stratosphere are the same persistent waves as observed in the MLT [*Chen et al*., 2016; *Chen and Chu*, 2017] and to infer the dominant wave propagation directions. A Doppler frequency shift exists between the intrinsic frequency $\hat{\omega}$ and the ground-relative frequency ω:

$$\hat{\omega} = \omega - \vec{k}\cdot\vec{\overline{u}} \cong \omega - \vec{k}_h\cdot\vec{\overline{u}}_h = \omega - k_h\overline{u}_h\cos\theta = \omega\left(1 - \frac{\overline{u}_h\cos\theta}{c_h}\right), \tag{6}$$

where $\vec{k}$ is the total wave vector, $\vec{\overline{u}}$ is the total mean background wind, $\vec{k}_h$ and $\vec{\overline{u}}_h$ are the horizontal wave and wind vectors, respectively. Considering the vertical mean background wind $|\overline{w}|$ is much smaller than the horizontal mean background wind $|\overline{u}_h|$, the vertical wind term is neglected in the second equality. θ is the angle between the wave propagation direction and the background wind, and $c_h = \omega/k_h = \lambda_h/\tau$ is the

horizontal phase speed of the gravity wave. Here $\tau = 2\pi/\omega$ is the ground-relative period, and $\lambda_h = 2\pi/k_h$ is the horizontal wavelength. As the intrinsic period $\hat{\tau}$ is given by

$$\hat{\tau} = \frac{2\pi}{\hat{\omega}} = \frac{2\pi}{\omega - k_h \overline{u}_h \cos\theta} = \frac{\tau}{1 - \frac{\overline{u}_h \cos\theta}{c_h}}, \tag{7}$$

the ground-relative period τ can be expressed precisely as

$$\tau = \hat{\tau}\left(1 - \frac{\overline{u}_h \cos\theta}{c_h}\right) = \hat{\tau}\left(1 - \frac{k_h \overline{u}_h \cos\theta}{\omega}\right). \tag{8}$$

Equation (8) gives roughly a linear relationship between the ground-relative period and the mean background wind $\overline{u}_h$, if $\hat{\tau}$, $\cos\theta$, and c_h do not change much, explaining the observations shown in Figures 7c and 7d. However, because the intrinsic period $\hat{\tau}$ can vary quite a bit under different background winds, deviations from the linear correlation are fairly visible in these two plots. Consequently, the slopes $S_\tau = -\frac{\hat{\tau}}{c_h}\cos\theta = -\frac{2\pi k_h \cos\theta}{\hat{\omega}\cdot\omega}$ in Figures 7c and 7d are subject to bias caused by the variations of $\hat{\tau}$.

According to the dispersion relation of inertial gravity waves including the Coriolis force but neglecting the term $\frac{1}{(4H^2)}$ (where H is the density scale height) [e.g., *Marks and Eckermann*, 1995; *Vadas*, 2013], the intrinsic angular frequency $\hat{\omega}$ obeys

$$\hat{\omega}^2 = \frac{{k_h}^2 N^2}{m^2} + f^2, \tag{9}$$

where N is the Brunt-Väisälä frequency in the unit of rad/s, k_h and m are the horizontal and vertical wave numbers, and $\lambda_h = 2\pi/k_h$ and $\lambda_z = 2\pi/m$ are respectively the horizontal and vertical wavelengths. The inertial frequency is $f = 2\Omega\sin\Theta$, where Ω is Earth's rotation rate and Θ is latitude. For McMurdo, the inertial period is $2\pi/f = 12.24$ h. Combining equations (6) and (9), we express the vertical wavelength as

$$\lambda_z = \frac{2\pi}{N}\sqrt{(c_h - \overline{u}_h \cos\theta)^2 - (f/k_h)^2}. \tag{10}$$

Equation (10) indicates that the relationship between λ_z and the mean background wind is rather complicated; however, we will demonstrate below that for the observed periods of 4–6 h in Figure 7, the Coriolis terms in equations (9) and (10) can be neglected, leading to a linear correlation between λ_z and the background wind. For this purpose, we define

$$\hat{\omega}_0 = N\left|\frac{k_h}{m}\right| = N\left|\frac{\lambda_z}{\lambda_h}\right| \text{ and } \hat{\tau}_0 = \frac{2\pi}{\hat{\omega}_0} \tag{11}$$

as the intrinsic angular frequency and intrinsic period, respectively, when the Coriolis term in equation (9) is omitted. Hence, the full intrinsic period can be written as

$$\hat{\tau} = \frac{2\pi}{\hat{\omega}} = \frac{2\pi}{\sqrt{{\hat{\omega}_0}^2 + f^2}} = \frac{1}{\sqrt{(1/\hat{\tau}_0)^2 + (f/2\pi)^2}} = \frac{1}{\sqrt{(1/\hat{\tau}_0)^2 + (1/12.24\text{ h})^2}}. \tag{12}$$

Equation (12) demonstrates that $\hat{\omega} > \hat{\omega}_0$ and $\hat{\tau} < \hat{\tau}_0$, but the corrections are quite small within the observed range in Figure 7. For example, for $\hat{\tau}_0 = 4$ h, $\hat{\tau} = 3.80$ h so the correction is ~5%; for $\hat{\tau}_0 = 6$ h, $\hat{\tau} = 5.39$ h and the correction is ~10%. Such small corrections for wave periods no more than 6 h are due to the square relation in equation (9), as the correction is approximately proportional to half of the square of period ratio:

$$\frac{\Delta\hat{\omega}}{\hat{\omega}_0} = \frac{\hat{\omega} - \hat{\omega}_0}{\hat{\omega}_0} \sim \frac{1}{2}\left(\frac{\hat{\tau}_0}{12.24\text{ h}}\right)^2. \tag{13}$$

Consequently, it is reasonable to neglect the Coriolis term in equations (9) and (10) for the waves with periods of ≤6 h, so we obtain a linear relationship between λ_z and the background wind

$$\lambda_z \approx \frac{2\pi}{N}(c_h - \overline{u}_h \cos\theta). \tag{14}$$

Equation (14) helps explain the observed linear correlation in Figures 6c and 6d. The slopes $S_{\lambda_z} = -\frac{2\pi\cos\theta}{N}$ in Figures 6c and 6d depend on N and $\cos\theta$.

To estimate the horizontal wavelengths and intrinsic periods of the stratospheric gravity waves, we use the following equations

$$\lambda_h = c_h \cdot \tau \approx c_h(\overline{u}_h \cos\theta = 0) \cdot \tau \tag{15}$$

$$\hat{\tau} = \frac{2\pi}{\hat{\omega}_0} = \frac{2\pi}{\left(\frac{\lambda_z}{\tau}\frac{N}{c_h}\right)} \approx \frac{2\pi}{N}\frac{c_h(\overline{u}_h \cos\theta = 0)}{\lambda_z/\tau}. \tag{16}$$

An assumption made in equations (15) and (16) is that the horizontal phase speed c_h does not change much for various background winds, so it is approximated as a constant at the point where the wind projection along the wave vector $\overrightarrow{k}_h$ is zero ($\overline{u}_h \cos\theta = 0$). This assumption is reasonable considering the vertical phase speed c_z remains nearly constant through the year in Figure 4c. Under this assumption, c_h can be derived from equation (14) as

$$c_h(\overline{u}_h \cos\theta = 0) = \frac{N \cdot \lambda_z(\overline{u}_h \cos\theta = 0)}{2\pi}. \tag{17}$$

Therefore, the final equations to derive the horizontal wavelengths and intrinsic periods are

$$\lambda_h \approx \frac{N \cdot \lambda_z(\overline{u}_h \cos\theta = 0) \cdot \tau}{2\pi} \tag{18}$$

$$\hat{\tau} \approx \frac{\lambda_z(\overline{u}_h \cos\theta = 0)}{\lambda_z/\tau}. \tag{19}$$

The $\cos\theta$ in equation (14) can be estimated from the fitted slopes in Figures 6c and 6d

$$\cos\theta = -\frac{S_{\lambda_z} \cdot N}{2\pi}. \tag{20}$$

The horizontal and vertical group velocities relative to the ground can be estimated using the intrinsic properties and background winds as [*Fritts and Alexander*, 2003; *Chen et al*., 2013]

$$c_{gh} = \frac{\partial\omega}{\partial k_h} = \frac{k_h\left(N^2 - \hat{\omega}^2\right)}{\hat{\omega}\left(k_h^2 + m^2 + 1/\left(4H^2\right)\right)} + \overline{u}_h \cos\theta \tag{21}$$

$$c_{gz} = \frac{\partial\omega}{\partial m} = -\frac{m\left(\hat{\omega}^2 - f^2\right)}{\hat{\omega}\left(k_h^2 + m^2 + 1/\left(4H^2\right)\right)} + \overline{w}, \tag{22}$$

where $\overline{u}_h$ and $\overline{w}$ are respectively the horizontal and vertical background winds, $H = 7$ km is the scale height of atmospheric density, and the vertical wave number m has negative and positive signs for the downward and upward phase progression waves, respectively. That is, when the background wind w is negligible, the energy propagation direction is opposite to the phase progression direction.

It is worth clarifying the convention usage on k_h, $\overline{u}_h$, and $\cos\theta$ in the above derivations. Our convention is that k_h is the (positive) magnitude of horizontal wave vector $\overrightarrow{k}_h$, the background wind $\overline{u}_h$ contains the sign information (not the absolute value), while $\cos\theta$ does not have the sign change and θ is defined as the angle from the positive wind direction to the wave vector $\overrightarrow{k}_h$ direction, regardless of the wind sign. In principle $\overrightarrow{u}$ in equation (6) is the total wind. Considering the vertical winds provided by ECMWF are at least 2–3 orders of magnitude smaller than the horizontal winds in the stratosphere, the vertical winds are neglected in all equations except equation (22). Also, because the meridional winds provided by ECMWF are in general much smaller than the zonal winds, we choose to use the zonal winds to represent the stratospheric horizontal winds. Defining the eastward as the positive zonal wind direction, the zonal winds plotted in Figures 6 and 7 have both positive and negative signs. Under such a convention, θ in above equations is defined as the

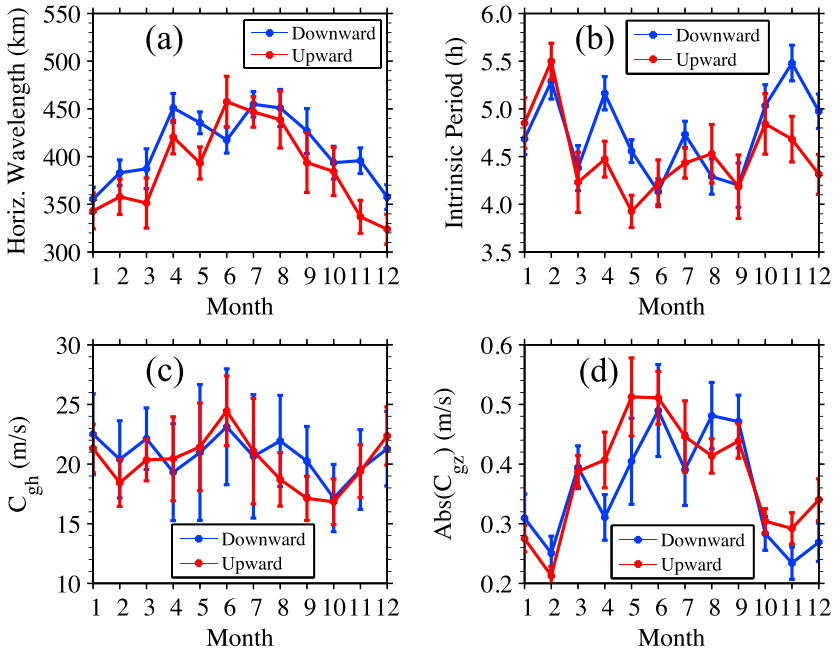

Figure 9. Inferred (a) horizontal wavelength, (b) intrinsic period, (c) ground-relative horizontal group velocity, and (d) the absolute value of vertical group velocity of the stratospheric gravity waves through 12 months of a year at McMurdo.

angle from the eastward to the wave vector $\vec{k}_h$, while $\overline{u}_h$ in equation (21) is the zonal wind with positive and negative signs, but not the magnitude only.

With equations (18)–(22) and the convention stated above, we estimate the intrinsic properties of gravity waves via plugging in actual numbers. As the intercepts in the zonal and meridional winds are comparable in Table 5 but the meridional cases have much larger uncertainties than the zonal cases, we infer λ_z $(\overline{u}_h \cos\theta = 0)$ only from the zonal wind plots. The vertical wavelengths at the zero wind points are inferred to be $\lambda_z(\overline{u}_h \cos\theta = 0) = 6.22$ km and $\lambda_z(\overline{u}_h \cos\theta = 0) = 6.11$ km for downward and upward phase progression waves, respectively. Taking the mean value of $N = 2.14 \times 10^{-2}$ rad/s derived from the lidar temperature data, we calculate the horizontal phase speeds to be $c_h(\overline{u}_h \cos\theta = 0) = 21.2$ m/s and $c_h(\overline{u}_h \cos\theta = 0) = 20.8$ m/s for the downward and upward phase progression waves, respectively. Substituting the monthly mean vertical wavelengths and ground-relative periods (as shown in Figures 4a and 4b) along with $\lambda_z(\overline{u}_h \cos\theta = 0)$ and $N = 2.14 \times 10^{-2}$ rad/s into equations (18) and (19), we estimate the horizontal wavelengths and intrinsic periods for all 12 months. The results are plotted in Figures 9a and 9b. The horizontal wavelengths are around 350–460 km, while the intrinsic periods are about 4–5 h. Using the slopes S_{λ_z} derived from the zonal wind plots (see Table 5), $\cos\theta$ derived from equation (20) are −0.14 and −0.16 for downward and upward phase progression waves, respectively. The horizontal and vertical group velocities are then estimated from equations (21) and (22) using the intrinsic properties and background winds, and the results are plotted in Figures 9c and 9d. The elevation angles of the energy propagation of the gravity waves calculated from the ratio of vertical to horizontal group velocities are about 1.1°, comparable to the case studies by *Chen et al.* [2013] in the MLT. Note that for downward (upward) phase progression waves, this elevation is for upward (downward) energy propagation.

The derived intrinsic periods are shorter than the corresponding ground-relative periods in most of the 12 months except the summer 4 months (November through February). When the zonal winds are eastward (positive) from March through October, negative $\cos\theta$ indicates that in the nonsummer months most gravity waves that survive at a given altitude (i.e., are not filtered out by the background wind) propagate against the background winds, leading to higher intrinsic frequencies. Consequently, the intrinsic periods are shorter than the ground-relative periods outside the summer months. During December, January, and February, the zonal winds are westward (negative). Negative $\cos\theta$ indicates that the dominant waves propagate along the background winds in summer, leading to lower intrinsic frequencies thus longer intrinsic periods than the

ground-relative counterparts. Because the horizontal winds in the winter stratosphere at McMurdo are dominated by the zonal winds, the small absolute values of $\cos\theta$ (0.14–0.16) indicate that the stratospheric gravity waves have their predominant propagating directions nearly along the north–south (meridional) directions.

In this section, the Doppler shift between the intrinsic and ground-relative frequencies as well as the dispersion relationship neglecting the Coriolis term help explain the linear correlations observed between the monthly mean vertical wavelengths/ground-relative periods and the monthly mean zonal wind velocities in the stratosphere. The linear relationships may reflect the critical level filtering effects; e.g., the orographic waves may be largely filtered out during summer months when the winds cross the zero point, while the strong eastward winds in winter may allow the orographic waves to propagate upward. Another factor is the extra wave generation in the stratosphere by the strong-wind-induced jet streams or unbalanced flow. Besides such speculations, the search of wave sources is beyond the scope of this study.

The derived horizontal wavelengths in the stratosphere are typically shorter than 500 km, which are significantly shorter than the dominant horizontal wavelengths in the MLT that are typically over 1000 km and up to several thousands of kilometers [*Chen et al*., 2013, 2016; *Chen and Chu*, 2017]. If we regard the horizontal wavelength of a gravity wave not changing much as the wave propagates upward in altitude, it is likely that the persistent gravity waves in the MLT region are not directly coming from the stratospheric dominant waves with the horizontal wavelengths of less than 500 km. Of course, we cannot rule out the possibility that some gravity waves in the tail of the lognormal distribution can penetrate to reach the MLT region. Another possibility is that some of the gravity waves propagating upward in the stratosphere dissipate between 40 and 65 km, which overlap with part of the gap region between the currently studied altitudes and the MLT altitudes studied by *Chen et al.* [2016]. Such dissipation results in horizontal body forces that generate upward and downward propagating secondary gravity waves [*Vadas et al*., 2003; E. Becker and S. L. Vadas, Northwest Research Associates, private communication, 2017]. These secondary waves usually have a wide spectral range, and, once propagating into the MLT, they become the important sources for the persistent and dominant 3–10 h waves discovered by lidar in the MLT region [*Chen et al*., 2016; *Chen and Chu*, 2017]. This speculation of possible wave sources in the lower to middle mesosphere may help explain the observations that the frequency spectral slopes in the lower mesosphere are much shallower than those in the MLT. This is because the upward propagating waves originated from the lower to middle mesosphere still carry some source spectra and have not dissipated sufficiently, thus contributing to the steeper slopes from 85 to 100 km (not far from the source) [*Chen et al*., 2016]; while the downward propagating waves originated from this source overlap with the upward propagating waves (from the lower atmosphere) around 60–65 km (right below the source region) with sufficient amplitudes, which may contribute to the shallower slopes as observed in this study. More observations are needed, especially in the gap region of 65–82 km, to investigate such possibilities.

7. Conclusions

Five years of atmospheric temperature data, measured with an Fe Boltzmann lidar by the University of Colorado group from 2011 to 2015 at Arrival Heights near McMurdo, Antarctica, are used to characterize the vertical wavelengths, periods, vertical phase speeds, frequency spectra, and vertical wave number spectra of stratospheric gravity waves from 30 to 50 km altitudes. A total of 1062 dominant gravity waves are identified from the data, allowing us to quantify the distributions of basic wave parameters. The seasonal distributions of vertical wavelengths, periods, and vertical phase speeds in summer, winter, and spring/fall are found obeying a lognormal distribution. The lognormal probability density function fittings to these distributions have nearly 100% correlation coefficients, making it unequivocal that the observed vertical wavelengths, periods, and vertical phase speeds are lognormally distributed at McMurdo. Both the downward and upward phase progression gravity waves are observed by the lidar, and the fractions of gravity waves with downward phase progression increase from summer ~59% to winter ~70%, similar to the lidar results for the South Pole and Rothera by *Yamashita et al.* [2009].

The seasonal and monthly mean vertical wavelengths and periods exhibit clear seasonal cycles with vertical wavelength growing from summer ~5.5 km to winter ~8.5 km, and period increasing from summer ~4.5 h to winter ~6 h. By analyzing the ECMWF wind data from 2011 through 2015, we discover statistically significant linear correlations between the monthly mean vertical wavelengths/periods and the mean zonal wind

velocities in the stratosphere. With larger stratospheric winds, gravity waves tend to have longer vertical wavelengths and longer ground-relative periods. Such linear correlations may be explained through the Doppler frequency shift of intrinsic frequency and dispersion relationship when neglecting the Coriolis term. This approximation of neglecting the Coriolis term introduces ~10% or less errors for gravity waves with periods not longer than 6 h, thus suitable for the McMurdo investigation.

By taking the vertical wavelengths at zero zonal wind points to estimate the horizontal phase speeds of ~21 m/s and assuming nearly constant horizontal phase speeds throughout the year, the monthly mean horizontal wavelengths, intrinsic periods, and horizontal and vertical group velocities are estimated for the stratospheric gravity waves through 12 months. The gravity waves reaching the McMurdo stratosphere (30–50 km) tend to have vertical wavelengths of ~6–8 km, horizontal wavelengths of ~350–460 km, intrinsic periods of ~4–5 h, and group velocities of ~22 m/s and ~0.45 m/s for the horizontal and vertical directions, respectively. Two interesting results further inferred are that the stratospheric gravity waves at McMurdo propagate along nearly the north-south direction with $|\cos\theta| \sim 0.14$, and the wave energy propagates at a very shallow elevation of ~1.1°.

Gravity wave frequency spectra show that the slopes between the characteristic frequency and 1 h^{-1} change from about −1.9 at 30–60 km to −1.45 around 60–65 km. The vertical wave number spectra exhibit that the power spectral densities at vertical wavelengths of ~5–20 km decrease from the winter maximum to the summer minimum. Because the typical horizontal wavelengths of dominant gravity waves in the stratosphere are substantially shorter than those of the dominant and persistent waves in the MLT region, we conclude that the typical dominant waves with horizontal wavelengths of ~350–460 km in the stratosphere are most likely not the direct source of the persistent gravity waves (3–10 h ground-relative periods and over 1000 km horizontal wavelengths) in the MLT observed by *Chen et al.* [2016] and *Chen and Chu* [2017]. However, it is possible that these stratospheric dominant waves dissipate in the upper stratosphere and mesosphere and generate secondary waves. These secondary waves as well as the gravity waves in the tail of the lognormal distribution may survive into the MLT, providing sources for the persistent waves in the MLT. Future observations and model simulations are required to solve these mysteries. Furthermore, wave intermittency and momentum flux may be inferred from the McMurdo lidar data as the potential subjects of future research. Such studies and parameters may help provide constraints to the GCM gravity wave parameterization.

Acknowledgments

We sincerely acknowledge Adrian J. McDonald and Chester S. Gardner for invaluable discussions on the gravity wave theory and characterization. We thank Zhangjun Wang, Wentao Huang, John A. Smith, Ian F. Barry, and Muzhou Lu for their contributions to the McMurdo lidar campaign. We are indebted to Vladimir Papitashvili and Julie Palais for their guidance and discussions. We are grateful to Richard Dean and Judy Shiple for their engineering help and support. We sincerely appreciate the staff of the United States Antarctic Program, McMurdo Station, Antarctica New Zealand, and Scott Base for their superb support over the years. We are grateful to the high-quality data from the European Centre for Medium Range Weather Forecasts (ECMWF) for this research. We thank Sharon L. Vadas and two other anonymous reviewers for their review comments that helped improve the manuscript quality. This project was supported by the National Science Foundation (NSF) grants ANT-0839091 and PLR-1246405. Xian Lu's research is supported by NSF grants AGS-1705448 (CEDAR) and PLR-1705450. Data necessary to reproduce the results are available from the authors upon request (xinzhao.chu@colorado.edu).

References

Alexander, M. J., and C. Barnet (2007), Using satellite observations to constrain parameterizations of gravity wave effects for global models, *J. Atmos. Sci.*, *64*, 1652–1665, doi:10.1175/JAS3897.1.

Alexander, M. J., and A. W. Grimsdell (2013), Seasonal cycle of orographic gravity wave occurrence above small islands in the Southern Hemisphere: Implications for effects on the general circulation, *J. Geophys. Res. Atmos.*, *118*, 11,589–11,599, doi:10.1002/2013JD020526.

Alexander, M. J., and J. R. Holton (2004), On the spectrum of vertically propagating gravity waves generated by a transient heat source, *Atmos. Chem. Phys.*, *4*(4), 923–932, doi:10.5194/acp-4-923-2004.

Alexander, M. J., and L. Pfister (1995), Gravity wave momentum flux in the lower stratosphere over convection, *Geophys. Res. Lett.*, *22*(15), 2029–2032, doi:10.1029/95GL01984.

Alexander, M. J., et al. (2008), Global estimates of gravity wave momentum flux from High Resolution Dynamics Limb Sounder observations, *J. Geophys. Res.*, *113*, D15S18, doi:10.1029/2007JD008807.

Alexander, M. J., et al. (2010), Recent developments in gravity-wave effects in climate models and the global distribution of gravity-wave momentum flux from observations and models, *Q. J. R. Meteorol. Soc.*, *136*, 1103–1124, doi:10.1002/qj.637.

Alexander, S. P., A. R. Klekociuk, and D. J. Murphy (2011), Rayleigh lidar observations of gravity wave activity in the winter upper stratosphere and lower mesosphere above Davis, Antarctica (69°S, 78°E), *J. Geophys. Res.*, *116*, D13109, doi:10.1029/2010JD015164.

Allen, S. J., and R. A. Vincent (1995), Gravity wave activity in the lower atmosphere: Seasonal and latitudinal variations, *J. Geophys. Res.*, *100*, 1327–1350, doi:10.1029/94JD02688.

Baumgaertner, A. J. G., and A. J. McDonald (2007), A gravity wave climatology for Antarctica compiled from challenging Minisatellite Payload/Global Positioning System (CHAMP/GPS) radio occultations, *J. Geophys. Res.*, *112*, D05103, doi:10.1029/2006JD007504.

Chen, C., and X. Chu (2017), Two-dimensional Morlet wavelet transform and its application to wave recognition methodology of automatically extracting two-dimensional wave packets from lidar observations in Antarctica, *J. Atmos. Sol.-Terr. Phys.*, doi:10.1016/j.jastp.2016.10.016.

Chen, C., X. Chu, A. J. McDonald, S. L. Vadas, Z. Yu, W. Fong, and X. Lu (2013), Inertia-gravity waves in Antarctica: A case study using simultaneous lidar and radar measurements at McMurdo/Scott Base (77.8°S, 166.7°E), *J. Geophys. Res. Atmos.*, *118*, 2794–2808, doi:10.1002/jgrd.50318.

Chen, C., X. Chu, J. Zhao, B. R. Roberts, Z. Yu, W. Fong, X. Lu, and J. A. Smith (2016), Lidar observations of persistent gravity waves with periods of 3–10 h in the Antarctic middle and upper atmosphere at McMurdo (77.83°S, 166.67°E), *J. Geophys. Res. Space Physics*, *121*, 1483–1502, doi:10.1002/2015JA022127.

Chu, X., and Z. Yu (2017), Formation mechanisms of neutral Fe layers in the thermosphere studied with a thermosphere-ionosphere Fe/Fe+ (TIFe) model in Antarctica, *J. Geophys. Res. Space Physics*, doi:10.1002/2016JA023773.

Chu, X., W. Pan, G. C. Papen, C. S. Gardner, and J. A. Gelbwachs (2002), Fe Boltzmann temperature lidar: Design, error analysis, and initial results at the North and South Poles, *Appl. Opt.*, *41*(21), 4400–4410, doi:10.1364/AO.41.004400.

Chu, X., P. J. Espy, G. J. Nott, J. C. Diettrich, and C. S. Gardner (2006), Polar mesospheric clouds observed by an iron Boltzmann lidar at Rothera (67.5°S, 68.0°W), Antarctica from 2002 to 2005: Properties and implications, *J. Geophys. Res.*, *111*, D20213, doi:10.1029/2006JD007086.

Chu, X., C. Yamashita, P. J. Espy, G. J. Nott, E. J. Jensen, H.-L. Liu, W. Huang, and J. P. Thayer (2009), Responses of polar mesospheric cloud brightness to stratospheric gravity waves at the South Pole and Rothera, Antarctica, *J. Atmos. Sol. Terr. Phys.*, *71*, 434–445, doi:10.1016/j.jastp.2008.10.002.

Chu, X., W. Huang, W. Fong, Z. Yu, Z. Wang, J. A. Smith, and C. S. Gardner (2011a), First lidar observations of polar mesospheric clouds and Fe temperatures at McMurdo (77.8°S, 166.7°E), Antarctica, *Geophys. Res. Lett.*, *38*, L16810, doi:10.1029/2011GL048373.

Chu, X., Z. Yu, C. S. Gardner, C. Chen, and W. Fong (2011b), Lidar observations of neutral Fe layers and fast gravity waves in the thermosphere (110-155 km) at McMurdo (77.8°S, 166.7°E), Antarctica, *Geophys. Res. Lett.*, *38*, L23807, doi:10.1029/2011GL050016.

Chu, X., Z. Yu, W. Fong, C. Chen, J. Zhao, I. F. Barry, J. A. Smith, X. Lu, W. Huang, and C. S. Gardner (2016), From Antarctica lidar discoveries to OASIS exploration, in *Proceedings of the 27th International Laser Radar Conference*, *EPJ Web of Conf.*, vol. 119, pp. 1–4, EPD Sci., New York, doi:10.1051/epjconf/201611912001.

Collins, R. L., and C. S. Gardner (1995), Gravity wave activity in the stratosphere and mesosphere at the South Pole, *Adv. Space Res.*, *16*(5), 81–90, doi:10.1016/0273-1177(95)00175-E.

Collins, R. L., A. Nomura, and C. S. Gardner (1994), Gravity waves in the upper mesosphere over Antarctica: Lidar observations at the South Pole and Syowa, *J. Geophys. Res.*, *99*(D3), 5475–5485, doi:10.1029/93JD03276.

Collins, R. L., T. J. Hallinan, R. W. Smith, and G. Hernandez (1996), Lidar observations of a large high-altitude sporadic Na layer during active aurora, *Geophys. Res. Lett.*, *23*(24), 3655–3658, doi:10.1029/96GL03337.

Dee, D. P., et al. (2011), The ERA-Interim reanalysis: Configuration and performance of the data assimilation system, *Q. J. R. Meteorol. Soc.*, *137*, 553–597, doi:10.1002/qj.828.

Dewan, E. M., and N. Grossbard (2000), Power spectral artifacts in published balloon data and implications regarding saturated gravity wave theories, *J. Geophys. Res.*, *105*(D4), 4667–4683, doi:10.1029/1999JD901108.

Eckermann, S. D., D. Broutman, J. Ma, J. D. Doyle, P.-D. Pautet, M. J. Taylor, K. Bossert, B. P. Williams, D. C. Fritts, and R. B. Smith (2016), Dynamics of orographic gravity waves observed in the mesosphere over the Auckland Islands during the Deep Propagating Gravity Wave Experiment (DEEPWAVE), *J. Atmos. Sci.*, *73*, 3855–3876, doi:10.1175/JAS-D-16-0059.1.

Espy, P. J., G. O. L. Jones, G. R. Swenson, J. Tang, and M. J. Taylor (2004), Seasonal variations of the gravity wave momentum flux in the Antarctic mesosphere and lower thermosphere, *J. Geophys. Res.*, *109*, D23109, doi:10.1029/2003JD004446.

Espy, P. J., R. E. Hibbins, G. R. Swenson, J. Tang, M. J. Taylor, D. M. Riggin, and D. C. Fritts (2006), Regional variations of mesospheric gravity-wave momentum flux over Antarctica, *Ann. Geophys.*, *24*, 81–88, doi:10.5194/angeo-24-81-2006.

Fong, W., X. Lu, X. Chu, T. J. Fuller-Rowell, Z. Yu, B. R. Roberts, C. Chen, C. S. Gardner, and A. J. McDonald (2014), Winter temperature tides from 30 to 110 km at McMurdo (77.8°S, 166.7°E), Antarctica: Lidar observations and comparisons with WAM, *J. Geophys. Res. Atmos.*, *119*, 2846–2863, doi:10.1002/2013JD020784.

Fritts, D. C., and M. J. Alexander (2003), Gravity wave dynamics and effects in the middle atmosphere, *Rev. Geophys., 41(1),* 1003, doi:10.1029/2001RG000106.

Fritts, D. C., S. L. Vadas, K. Wan, and J. A. Werne (2006), Mean and variable forcing of the middle atmosphere by gravity waves, *J. Atmos. Sol. Terr. Phys.*, *68*, 247–265, doi:10.1016/j.jastp.2005.04.010.

Garcia, R. R., M. López-Puertas, B. Funke, D. R. Marsh, D. E. Kinnison, A. K. Smith, and F. González-Galindo (2014), On the distribution of CO_2 and CO in the mesosphere and lower thermosphere, *J. Geophys. Res. Atmos.*, *119*, 5700–5718, doi:10.1002/2013JD021208.

Gardner, C. S., D. C. Senfit, T. J. Beatty, R. E. Bills, and C. A. Hostetler (1989), Rayleigh and sodium lidar techniques for measuring middle atmospheric density, temperature and wind perturbations and their spectra, in *World Ionosphere/Thermosphere Study Handbook*, vol. 2, edited by C. H. Liu and B. Edwards, pp. 148–187, Int. Congr. of Sci. Unions, Urbana, Ill.

Gong, J., D. L. Wu, and S. D. Eckermann (2012), Gravity wave variances and propagation derived from AIRS radiances, *Atmos. Chem. Phys.*, *12*, 1701–1720, doi:10.5194/acp-12-1701-2012.

Hamilton, K., R. J. Wilson, and R. S. Hemler (1999), Middle atmosphere simulated with high vertical and horizontal resolution versions of a GCM: Improvements in the cold pole bias and generation of a QBO-like oscillation in the tropics, *J. Atmos. Sci.*, *56*, 3829–3846, doi:10.1175/1520-0469(1999)056,3829:MASWHV.2.0.CO;2.

Hertzog, A., et al. (2007), Stratéole/Vorcore—Long-duration, superpressure balloons to study the Antarctic lower stratosphere during the 2005 winter, *J. Atmos. Oceanic Tech.*, *24*, 2048–2061, doi:10.1175/2007JTECHA948.1.

Hertzog, A., G. Boccara, R. A. Vincent, F. Vial, and P. Cocquerez (2008), Estimation of gravity wave momentum flux and phase speeds from quasi-Lagrangian stratospheric balloon flights. Part II: Results from the VORCORE campaign in Antarctica, *J. Atmos. Sci.*, *65*, doi:10.1175/2008JAS2710.1.

Hertzog, A., M. J. Alexander, and R. Plougonven (2012), On the intermittency of gravity wave momentum flux in the stratosphere, *J. Atmos. Sci.*, *69*(11), 3433–3448, doi:10.1175/JAS-D-12-09.1.

Hibbins, R. E., P. J. Espy, M. J. Jarvis, D. M. Riggin, and D. C. Fritts (2007), A climatology of tides and gravity wave variance in the MLT above Rothera, Antarctica obtained by MF radar, *J. Atmos. Sol. Terr. Phys.*, *69*(4–5), 578–588, doi:10.1016/j.jastp.2006.10.009.

Hines, C. O. (1960), Internal atmospheric gravity waves at ionospheric heights, *Can. J. Phys.*, *38*, 1441, doi:10.1139/p60-150.

Hines, C. O. (1964), Minimum vertical scale sizes in the wind structure above 100 kilometers, *J. Geophys. Res.*, *69*(13), 2847–2848, doi:10.1029/JZ069i013p02847.

Hines, C. O. (1974), *The Upper Atmosphere in Motion*, pp. 13–344, AGU, Washington, D. C., doi:10.1029/GM018p0014.

Hitchman, M. H., J. C. Gille, C. D. Rodgers, and G. Brasseur (1989), The separated polar winter stratopause: A gravity wave driven climatological feature, *J. Atmos. Sci.*, *46*, 410–422, doi:10.1175/1520-0469(1989)046%3C0410:TSPWSA%3E2.0.CO;2.

Hoffmann, L., and M. J. Alexander (2009), Retrieval of stratospheric temperatures from Atmospheric infrared Sounder radiance measurements for gravity wave studies, *J. Geophys. Res.*, *114*, D07105, doi:10.1029/2008JD011241.

Hoffmann, L., X. Xue, and M. J. Alexander (2013), A global view of stratospheric gravity wave hotspots located with Atmospheric Infrared Sounder observations, *J. Geophys. Res. Atmos.*, *118*, 416–434, doi:10.1029/2012JD018658.

Hoffmann, L., A. W. Grimsdell, and M. J. Alexander (2016), Stratospheric gravity waves at southern Hemisphere orographic hotspots: 2003–2014 AIRS/Aqua observations, *Atmos. Chem. Phys.*, *16*, 9381–9397, doi:10.5194/acp-16-9381-2016.

Holton, J. R. (1982), The role of gravity wave induced drag and diffusion in the momentum budget of the mesosphere, *J. Atmos. Sci.*, *39*, 791–799, doi:10.1175/1520-0469(1982)039<0791:TROGWI>2.0.CO;2.

Hostetler, C. A., and C. S. Gardner (1994), Observations of horizontal and vertical wave number spectra of gravity wave motions in the stratosphere and mesosphere over the mid-Pacific, *J. Geophys. Res.*, *99*(D1), 1283–1302, doi:10.1029/93JD02927.

Kaifler, B., F.-J. Lübken, J. Höffner, R. J. Morris, and T. P. Viehl (2015), Lidar observations of gravity wave activity in the middle atmosphere over Davis (69°S, 78°E), Antarctica, *J. Geophys. Res. Atmos.*, *120*, 4506–4521, doi:10.1002/2014JD022879.

Kim, Y.-J., S. D. Eckermann, and H.-Y. Chun (2003), An overview of the past, present and future of gravity wave drag parameterization for numerical climate and weather prediction models, *Atmos. Ocean*, *41*, 65–98, doi:10.3137/ao.410105.

Lee, Y., D. Shindell, G. Faluvegi, M. Wenig, Y. Lam, Z. Ning, S. Hao, and C. Lai (2014), Increase of ozone concentrations, its temperature sensitivity and the precursor factor in South China, *Tellus Ser. B*, *66*, doi:10.3402/tellusb.v66.23455.

Lindzen, R. S. (1981), Turbulence and stress owing to gravity wave and tidal breakdown, *J. Geophys. Res.*, *86*(C10), 9707–9714, doi:10.1029/JC086iC10p09707.

Liu, H.-L., J. M. McInerney, S. Santos, P. H. Lauritzen, M. A. Taylor, and N. M. Pedatella (2014), Gravity waves simulated by high-resolution Whole Atmosphere Community Climate Model, *Geophys. Res. Lett.*, *41*, 9106–9112, doi:10.1002/2014GL062468.

Lu, X., X. Chu, T. Fuller-Rowell, L. Chang, W. Fong, and Z. Yu (2013), Eastward propagating planetary waves with periods of 1–5 days in the winter Antarctic stratosphere as revealed by MERRA and lidar, *J. Geophys. Res. Atmos.*, *118*, 9565–9578, doi:10.1002/jgrd.50717.

Lu, X., X. Chu, W. Fong, C. Chen, Z. Yu, B. R. Roberts, and A. J. McDonald (2015a), Vertical evolution of potential energy density and vertical wave number spectrum of Antarctic gravity waves from 35 to 105 km at McMurdo (77.8°S, 166.7°E), *J. Geophys. Res. Atmos.*, *120*, 2719–2737, doi:10.1002/2014JD022751.

Lu, X., C. Chen, W. Huang, J. A. Smith, X. Chu, T. Yuan, P.-D. Pautet, M. J. Taylor, J. Gong, and C. Y. Cullens (2015b), A coordinated study of 1 h mesoscale gravity waves propagating from Logan to Boulder with CRRL Na Doppler lidars and temperature mapper, *J. Geophys. Res. Atmos.*, *120*, 10,006–10,021, doi:10.1002/2015JD023604.

Lu, X., X. Chu, H. Li, C. Chen, J. Smith, and S. Vadas (2016), Statistical characterization of high-to-medium frequency mesoscale gravity waves by lidar-measured vertical winds and temperatures in the MLT, *J. Atmos. Sol. Terr. Phys.*, doi:10.1016/j.jastp.2016.10.009.

Marks, C. J., and S. D. Eckermann (1995), A three-dimensional non-hydrostatic ray-tracing model for gravity waves: Formulation and preliminary results for the middle atmosphere, *J. Atmos. Sci.*, *52*, 1959–1984, doi:10.1175/1520-0469(1995)052<1959:ATDNRT>2.0.CO;2.

McDonald, A. J., S. E. George, and R. M. Woollands (2009), Can gravity waves significantly impact PSC occurrence in the Antarctic?, *Atmos. Chem. Phys.*, *9*, 8825–8840, doi:10.5194/acp-9-8825-2009.

McLandress, C., W. E. Ward, V. I. Fomichev, K. Semeniuk, S. R. Beagley, N. A. McFarlane, and T. G. Shepherd (2006), Large-scale dynamics of the mesosphere and lower thermosphere: An analysis using the extended Canadian Middle Atmosphere Model, *J. Geophys. Res.*, *111*, D17111, doi:10.1029/2005JD006776.

McLandress, C., T. G. Shepherd, S. Polavarapu, and S. R. Beagley (2012), Is missing orographic gravity wave drag near 60°S the cause of the stratospheric zonal wind biases in chemistry–climate models?, *J. Atmos. Sci.*, *69*(3), 802–818, doi:10.1175/JAS-D-11-0159.1.

Moffat-Griffin, T., R. E. Hibbins, M. J. Jarvis, and S. R. Colwell (2011), Seasonal variations of gravity wave activity in the lower stratosphere over an Antarctic Peninsula station, *J. Geophys. Res.*, *116*, D14111, doi:10.1029/2010JD015349.

Moffat-Griffin, T., M. J. Jarvis, S. R. Colwell, A. J. Kavanagh, G. L. Manney, and W. H. Daffer (2013), Seasonal variations in lower stratospheric gravity wave energy above the Falkland Islands, *J. Geophys. Res. Atmos.*, *118*, 10,861–10,869, doi:10.1002/jgrd.50859.

Murphy, D. J., S. P. Alexander, A. R. Klekociuk, P. T. Love, and R. A. Vincent (2014), Radiosonde observations of gravity waves in the lower stratosphere over Davis, Antarctica, *J. Geophys. Res. Atmos.*, *119*, 11,973–11,996, doi:10.1002/2014JD022448.

Mzé, N., A. Hauchecorne, P. Keckhut, and M. Thétis (2014), Vertical distribution of gravity wave potential energy from long-term Rayleigh lidar data at a northern middle-latitude site, *J. Geophys. Res. Atmos.*, *119*, 12,069–12,083, doi:10.1002/2014JD022035.

Press, W. H., B. P. Flannery, S. A. Teukolsky, and W. T. Vetterling (1986), *Numerical Recipes: The Art of Scientific Computing*, pp. 454–497, Cambridge Univ. Press, New York.

Rabier, F., et al. (2012), The Concordiasi field experiment over Antarctica: First results from innovative atmospheric measurements, *Bull. Am. Meteorol. Soc.*, *94*, ES17–ES20, doi:10.1175/BAMS-D-12-00005.1.

Richter, J. H., F. Sassi, and R. R. Garcia (2010), Towards a physically based gravity wave source parameterization in a general circulation model, *J. Atmos. Sci.*, *67*, 136–156, doi:10.1175/2009JAS3112.1.

Sato, K., and M. Yoshiki (2008), Gravity wave generation around the polar vortex in the stratosphere revealed by 3-hourly radiosonde observations at Syowa Station, *J. Atmos. Sci.*, *65*(12), 3719–3735, doi:10.1175/2008jas2539.1.

Senft, D. C., and C. S. Gardner (1991), Seasonal variability of gravity wave activity and spectra in the mesopause region at Urbana, *J. Geophys. Res.*, *96*, 17,229–17,264, doi:10.1029/91JD01662.

Smith, R. B., et al. (2016), Stratospheric gravity wave fluxes and scales during DEEPWAVE, *J. Atmos. Sci.*, *73*, 2851–2869, doi:10.1175/JAS-D-15-0324.1.

Steele, H. M., P. Hamill, M. P. McCormick, and T. J. Swissler (1983), The formation of polar stratospheric clouds, *J. Atmos. Sci.*, *40*, 2055–2068, doi:10.1175/1520-0469(1983)040<2055:TFOPSC>2.0.CO;2.

Tan, B. (2012), Observational and modeling study of polar middle atmosphere dynamics and thermal structures, PhD dissertation, Univ. of Colorado Boulder, Boulder, Colo.

Tsuda, T., M. Nishida, C. Rocken, and R. H. Ware (2000), A global morphology of gravity wave activity in the stratosphere revealed by the GPS occultation data (GPS/MET), *J. Geophys. Res.*, *105*(D6), 7257–7273, doi:10.1029/1999JD901005.

Vadas, S. L. (2013), Compressible *f*-plane solutions to body forces, heatings, and coolings, and application to the primary and secondary gravity waves generated by a deep convective plume, *J. Geophys. Res. Space Physics*, *118*, 2377–2397, doi:10.1002/jgra.50163.

Vadas, S. L., D. C. Fritts, and M. J. Alexander (2003), Mechanism for the generation of secondary waves in wave breaking regions, *J. Atmos. Sci.*, *60*, 194–214, doi:10.1175/1520-0469(2003)060<0194:MFTGOS>2.0.CO;2.

Vadas, S. L., M. J. Taylor, P.-D. Pautet, P. A. Stamus, D. C. Fritts, H.-L. Liu, F. T. São Sabbas, V. T. Rampinelli, P. Batista, and H. Takahashi (2009), Convection: The likely source of medium-scale gravity waves observed in the OH airglow layer near Basilia, Brazil, during the SpreadFEx campaign, *Ann. Geophys.*, *27*, 231–259.

Walterscheid, R. L., L. J. Gelinas, C. R. Mechoso, and G. Schubert (2016), Spectral distribution of gravity wave momentum fluxes over the Antarctic Peninsula from Concordiasi superpressure balloon data, *J. Geophys. Res. Atmos.*, *121*, 7509–7527, doi:10.1002/2015JD024253.

Wang, Z., X. Chu, W. Huang, W. Fong, J. A. Smith, and B. Roberts (2012), Refurbishment and upgrade of Fe Boltzmann/Rayleigh temperature lidar at Boulder for McMurdo lidar campaign in Antarctica, in *Proceeding of the 26th International Laser Radar Conference*, pp. 207–210, Porto Heli, Greece, 25–29 June.

Whiteway, J. A., T. J. Duck, D. P. Donovan, J. C. Bird, S. R. Pal, and A. I. Carswell (1997), Measurements of gravity wave activity within and around the Arctic stratospheric vortex, *Geophys. Res. Lett.*, *24*, 1387–1390, doi:10.1029/97GL01322.

Yamashita, C., X. Chu, H.-L. Liu, P. J. Espy, G. J. Nott, and W. Huang (2009), Stratospheric gravity wave characteristics and seasonal variations observed by lidar at the South Pole and Rothera, Antarctica, *J. Geophys. Res.*, *114*, D12101, doi:10.1029/2008JD011472.

York, D., N. Evensen, M. Martinez, and J. Delgado (2004), Unified equations for the slope, intercept, and standard errors of the best straight line, *Am. J. Phys.*, *72*, 367–375, doi:10.1119/1.1632486.

Yoshiki, M., and K. Sato (2000), A statistical study of gravity waves in the polar regions based on operational radiosonde data, *J. Geophys. Res.*, *105*(D14), 17,995–18,011, doi:10.1029/2000JD900204.

Zhu, X., and J. R. Holton (1987), Mean fields induced by local gravity-wave forcing in the middle atmosphere, *J. Atmos. Sci.*, *44*, 620–630, doi:10.1175/1520-0469(1987)044<0620:MFIBLG>2.0.CO;2.